NUMERICAL SIMULATION OF BREAKING WAVES

USING LEVEL-SET NAVIER-STOKES METHOD

A Thesis

by

Qian Dong

Submitted to the Office of Graduate Studies of
Texas A&M University
in partial fulfillment of the requirements for the degree of

MASTER OF SCIENCE

May 2010

Major Subject: Civil Engineering

NUMERICAL SIMULATION OF BREAKING WAVES

USING LEVEL-SET NAVIER-STOKES METHOD

A Thesis

by

QIAN DONG

Submitted to the Office of Graduate Studies of
Texas A&M University
in partial fulfillment of the requirements for the degree of

MASTER OF SCIENCE

Approved by:

Chair of Committee,	Hamn-Ching Chen
Committee Members,	Alan Palazzolo
	Jun Zhang
Head of Department,	John Niedzwecki

May 2010

Major Subject: Civil Engineering

ABSTRACT

Numerical Simulation of Breaking Waves using

Level-Set Navier-Stokes Method. (May 2010)

Qian Dong, B.S., Zhejiang University

Chair of Advisory Committee: Dr. Hamn-Ching Chen

In the present study, a fifth-order weighted essentially non-oscillatory (WENO) scheme was built for solving the surface-capturing level-set equation. Combined with the level-set equation, the three-dimensional Reynolds averaged Navier-Stokes (RANS) equations were employed for the prediction of nonlinear wave-interaction and wave-breaking phenomena over sloping beaches.

In the level-set finite-analytic Navier-Stokes (FANS) method, the free surface is represented by the zero level-set function, and the flows are modeled as immiscible air-water two phase flows. The Navier-Stokes equations for air-water two phase flows are formulated in a moving curvilinear coordinate system and discretized by a 12-point finite-analytical scheme using the finite-analytic method on a multi-block over-set grid system. The Pressure Implicit with Splitting of Operators / Semi-Implicit Method for Pressure-Linked Equation Revised (PISO/SIMPLER) algorithm was used to determine the coupled velocity and pressure fields. The evolution of the level-set method was solved using the third-order total variation diminishing (TVD) Runge-Kutta method and

fifth-order WENO scheme. The accuracy was confirmed by solving the Zalesak's problem.

Two major subjects are discussed in the present study. First, to identify the WENO scheme as a more accurate scheme than the essentially non-oscillatory scheme (ENO), the characteristics of a nonlinear monochromatic wave were studied systematically and comparisons of wave profiles using the two schemes were conducted. To eliminate other factors that might produce wave profile fluctuation, different damping functions and grid densities were studied. To damp the reflection waves efficiently, we compared five damping functions. The free-surface elevation data collected from gauges distributed evenly in a numerical wave tank are analyzed to demonstrate the damping effect of the beach.

Second, as a surface-tracking numerical method built on curvilinear coordinates, the level-set RANS model was tested for nonlinear bichromatic wave trains and breaking waves on a sloping beach with a complex free surface. As the wave breaks, the velocity of the fluid flow surface became more complex. Numerical modeling was performed to simulate the two-phase flow velocity and its corresponding surface and evolution when the wave passed over different sloping beaches. The breaking wave test showed that it is an efficient technique for accurately capturing the breaking wave free surface. To predict the breaking points, different wave heights and beach slopes are simulated. The results show that the dependency of wave shape and breaking characteristics to wave height and beach slope match the results provided by experiments.

ACKNOWLEDGEMENTS

I would like to offer my sincerest gratitude to my supervisor, Dr. Hamn-Ching Chen, who has supported me throughout my thesis with his patience and knowledge, allowing me the room to work in my own way. I attribute the level of my Masters degree to his encouragement and generous instruction. Without him, this thesis would not have been written or completed. All my work is based on Dr. Chen's research, from which I was given access to research this topic. In the final stages of the work, Dr. Chen also has been abundantly helpful, and has assisted me in numerous ways, including summarizing the contents.

I would like to extend my gratefulness to my committee, Dr. Jun Zhang, and Dr. Alan Palazzolo for their valuable time, suggestions and personal encouragements.

To my parents and my whole family I am truly grateful. Their boundless love and support has always been my spiritual power and inspiration.

TABLE OF CONTENT

Page

ABSTRACT iii

ACKNOWLEDGEMENTS v

TABLE OF CONTENTS vi

LIST OF FIGURES viii

LIST OF TABLES xi

CHAPTER

I INTRODUCTION 1

Background 1
Numerical Simulation of Overturning Wave Using Level-Set Method 2
Boundary Conditions and Buffer Domain Treatment 5
Presentation Outline 6

II GOVERNING EQUATIONS 8

Introduction 8
Level-Set Method 8
RANS Equations 11
Velocity Extrapolation 15

III NUMERICAL EQUATION 17

IV VERIFICATION OF PRESENT MODEL 20

Zalesak's Problem 20
Monochromic Wave Propagation 23
Experimental Setup 24
Buffer Domain Treatment 25
Grid Refinement Study 40

CHAPTER Page

V BICHROMATIC WAVE INTERACTION AND EVOLUTION OF A BREAKING WAVE OVER A SLOPING BEACH 47

Interaction of Bichromatic Waves in a Flat Flume 47
Evolution of Breaking Waves over a Sloping Beach 57

VI CONCLUSIONS 69

REFERENCES 71

VITA 77

LIST OF FIGURES

		Page
Figure 1	Zalesak's Problem: velocity field	21
Figure 2	Zalesak's Problem: initial position and contour plot of ϕ	21
Figure 3	Zalesak's Problem: uniform grid in domain 100*100	22
Figure 4	Zalesak's Problem: comparison of predicted interfaces at t = 0, 157, 314, 471 and 628, using HJENO and WENO scheme	23
Figure 5	2D schematic diagram for wave maker	24
Figure 6	Schematic of buffer zone implementation	28
Figure 7	Typical mesh for 2D wave maker (Refine mesh near the free surface)	29
Figure 8	Computational domain for 2D wave maker	29
Figure 9	Shape of five damping functions tested within the buffer domain.	30
Figure 10	Test 1: Wave profile and velocity distribution at t = 5.7T	31
Figure 11	Test 1: Wave profile at consequent time (t = 11.8T, 11.9T, 12.0T, 12.1T, 12.2T, 12.3T and 12.4T)	31
Figure 12	Test 2: Wave profile and velocity distribution at t = 5.7T	32
Figure 13	Test 2: Wave profile at consequent time (t = 11.8T, 11.9T, 12.0T, 12.1T, 12.2T, 12.3T and 12.4T)	33
Figure 14	Comparison of Test 1 and Test 2	33
Figure 15	Test 3: Wave profile and velocity distribution at t = 5.7T	34
Figure 16	Test 3: Wave profile at consequent time (t = 11.8T, 11.9T, 12.0T, 12.1T, 12.2T, 12.3T and 12.4T)	34
Figure 17	Test 4: Wave profile and velocity distribution at t = 5.7T	36

Page

Figure 18	Test 4: Wave profile at consequent time (t = 11.8T, 11.9T, 12.0T, 12.1T, 12.2T, 12.3T and 12.4T)	36
Figure 19	Test 5: Wave profile and velocity distribution at t = 5.7T	37
Figure 20	Test 5: Wave profile at consequent time (t = 11.8T, 11.9T, 12.0T, 12.1T, 12.2T, 12.3T and 12.4T)	37
Figure 21	Test 6: Wave profile and velocity distribution at t = 5.7T	38
Figure 22	Test 6: Wave profile at consequent time (t = 11.8T, 11.9T, 12.0T, 12.1T, 12.2T, 12.3T and 12.4T)	39
Figure 23	Comparison of Test 2 and Test 6	39
Figure 24	Schematic of wave flume and buffer zone implementation	41
Figure 25	Wave profile on different grid for Test 1 and Test 2	42
Figure 26	Comparison of wave elevations at three gages for different type of grid sizes	44
Figure 27	Time history of wave profile for WENO and ENO-3rd scheme on Grid Case 1	45
Figure 28	Time series of free surface elevation at different locations.....	46
Figure 29	Numerical grid for bichromatic wave interaction case	49
Figure 30	Flume Configuration	49
Figure 31	Schematic of Program DWS and buffer zone implementation	50
Figure 32	Comparison of single wave and group wave computed by DWS and RANS.....	51
Figure 33	Sinusoidal input (left-hand column) and simulation using RANS (right-hand column) surface elevation	52
Figure 34	The interaction between two nonlinear waves	54

Page

Figure 35 Comparison of single nonlinear waves superposition and simulation free surface 55

Figure 35 (continued) 56

Figure 36 Sketch for model set up on sloping beach 58

Figure 37 Typical mesh for 2D surf zone (Refine mesh near the free surface) 58

Figure 38 Wave shape at consequent time (Case 2) 60

Figure 39 Propagation of the second wave crest on beaches with slope 1/15 and 1/20 (H_0=0.57) 62

Figure 40 Propagation of the third wave crest on beaches with slope 1/15 and 1/20 (H_0=0.57) 63

Figure 41 Propagation of the second wave crest on beaches with slope 1/15 and 1/20 (H_0=0.65) 64

Figure 42 Propagation of the third wave crest on beaches with slope 1/15 and 1/20 (H_0=0.65) 65

Figure 43 Propagation of the second wave crest on beaches with slope 1/15 and 1/20 (H_0=0.70) 66

Figure 44 Propagation of the third wave crest on beaches with slope 1/15 and 1/20 (H_0=0.70) 67

Figure 44 (Continued) 68

LIST OF TABLES

Page

Table 1 Locations of wave elevation measurement 28

Table 2 Grid density for Test 1 and Test 2 41

Table 3 Grid density for Case 1, Case 2 and Case 3 43

Table 4 Slope and input wave height for all cases 59

Table 5 Breaking characteristics 61

CHAPTER I

INTRODUCTION

Background

On Sept. 13, 2008, Hurricane Ike struck the Texas coast near Galveston. After inspection, severe beach erosion and prominent over-wash fans were observed throughout the study area. (Ewing et al., 2009) It is well known that hurricanes can cause severe damage due to the extremely high winds, storm surge and breaking waves. Currents induced by breaking waves are the driving mechanism for sediment transport, which leads to beach erosion and accretion. An accurate study of the wave-breaking process in the surf zone is particularly important in understanding erosion problems and impact forces on offshore and near-shore structures.

The wave-breaking process is a highly nonlinear phenomenon involving two-phase flow and turbulent flow. The greatest difficulties in the simulation of wave breaking are in the calculation of the free-surface profile. Conventionally, free surface is assumed to be continuous and is a material surface in numerical models. However, these are no longer valid in breaking waves (Lin and Liu, 1998a). Most existing numerical models are not capable of obtaining accurate solutions for the free surface of breaking waves. They simulate the breaking process by adding a dissipation term to the depth-integrated momentum equations so that the velocity field is invalid. Moreover, turbulent kinetic energy is inadequately performed in these models.

This thesis follows the style of *American Society of Civil Engineering Journal*.

More recently, the numerical simulation of unsteady waves has improved significantly. The present stage of Navier-Stokes equations-based numerical modeling of breaking waves can be classified into three levels: (I) those that solve the Navier-Stokes equations directly, contain no turbulence models (Miyata, 1986), or include constant eddy viscosity in both space and time (Petit et al., 1994); (II) those that solve the RANS equations (Lemos, 1992; Lin and Liu, 1998a; Lin and Liu, 1998b; Bradford, 2000, and Christensen et al., 2000); (III) and those that solve the space-filtered Navier-Stokes equations (Zhao and Tanimoto, 1998; Wijayaratna and Okayasu, 2000; Christensen and Deigaard, 2001). In the present study, the level-set finite-analytic Navier-Stokes (FANS) method of Chen and Yu is employed for capturing the breaking-wave surface. This method was generalized from the chimera RANS method of Chen and Chen (1998) and Chen et al. (2000) to incorporate an interface-capturing method based on the level-set method of Osher and Sethian (1988). For purposes of discussion, we present the techniques in the context of wave breaking over a sloping beach.

Numerical Simulation of an Overturning Wave Using the Level-Set Method

The numerical models of breaking waves can be classified into two methods: the interface-tracking method and the interface-capturing method (Ferziger and Peric, 1999). The interface-tracking method follows the free surface motions and uses boundary-fitted grids that are readjusted in each time step whenever the free surface moves. The interface-capturing method does not define a sharp free-surface boundary. Instead, the computation is performed on a fixed grid, which is extended beyond the free surface and the shape of this free surface is determined by cells that are partially filled. A variety of

numerical methods in this interface-capturing approach have been developed over the past several decades. Among them, numerical models based on solving the full Navier-Stokes equation have become increasingly popular. This approach can provide full details of the flow in the surf zone, ranging from the breaking process to bore formation, run-up, and backwash. One of the difficulties in breaking wave simulation is free surface tracking because the free surface is set on an arbitrary moving boundary. Three typical methods for this approach are the marker and cell (MAC) scheme (Harlow and Welch, 1965), volume of fluid (VOF) scheme (Nichols et al., 1980; Hirt and Nichols, 1981), and the level-set method (Osher and Sethian, 1988).

The MAC method presented by Harlow and Welch (1965) was the first attempt made to simulate the time-dependent viscous, incompressible fluid flow with a free surface. A finite difference technique was used to discrete incompressible, two-dimensional Navier-Stokes equations on a uniform Cartesian-staggered grid system and the velocity boundary conditions at the free surface are based upon the requirement of mass conservation. The essential principal concept of free surface advancement in the MAC method is that the coordinates of marker particles distributed everywhere in the computational domain are assumed to be known at the beginning and moved according to the velocity components in their vicinities. Subsequently, improved versions about this Lagrangian technique have been reported; e.g., SMAC (Amsden and Harlow, 1970), SM (Chen et al., 1991), and GENSMAC (Tome and Mckee, 1994) etc.

Opposite to the Lagrangian technique mentioned previously, the VOF method originally proposed and developed by Hirt and Nichols (1981) was based on the Eulerian

principle. This method can simulate complex free surfaces, including fluid merging and reconnection. Locating the free surface is accomplished by using a specific function defined as the fractional volume ratio of the cell occupied by fluid. The modified versions of VOF method have been widely used to track the interfaces between different fluids.

Recently, a novel technique presented by Sussman et al. (1994) was derived for computing the motion of two-phase flow that allows for large density ratios, surface tension and jumps in viscosity. A level-set method (Osher and Sethian, 1988) was proposed for capturing the interface between two fluids, and can be generalized easily to three-dimensional problems. This new treatment of the level-set method provides another way to compute the interface separation and combination such as the motion of air bubbles in water or falling water drops in air. However, numerical diffusion can arise as the time advances. Numerous researchers such as Sussman et al. (1998), Peng et al. (1999), Sethian (2001), and Enright et al. (2002) attempted to modify the traditional level-set method and develop a more accurate and efficient solution algorithm to reduce the computational effort.

In the present study, we used the level-set method in conjunction with the chimera RANS method of Chen and Chen (1998). The governing equations are formulated in a curvilinear coordinate system and discretized using the finite-analytic method of Chen et al. (1990) A numerical wave tank model was developed to simulate the propagating wave over a sloping beach. To generate the anticipated waves, a piston-type wave maker was located upstream from the wave. The evolution of the level-set method was solved

using the third-order TVD Runge-Kutta method (Yue et al., 2003) and fifth-order WENO scheme (Liu, Osher, and Chan, 1994).

Boundary Conditions and Buffer Domain Treatment

For numerical simulations of viscous compressible flow, most models are performed using periodic boundary conditions in the stream-wise direction. This kind of "temporal setting" needs only a relatively small computational domain in the stream-wise direction. The periodicity assumption, which limits the applicability of these simulations, has been directly compared with physical experiments (Wasistho, 1997). To make the model much more general, we need to identify a more general setting where there is no periodicity in the stream-wise direction; therefore, artificial inflow and outflow boundaries are needed.

Another computational reference frame called a "spatial setting" is fixed in space where the flow enters the domain through the inflow boundary and leaves through the outflow boundary. The major drawback of this type of simulation is that the computational effort is considerably more demanding because a much larger stream-wise extent of the computational domain is required. Also, it is difficult for these spatial simulations to generate consistent and accurate inflow and outflow boundary conditions. The boundary conditions should be consistent to ensure the well-posedness of the Navier-Stokes equations. On the other hand, an outflow boundary condition is needed to prevent spurious numerical reflections as much as possible that can disturb the solution within the domain. Stable outflow boundary conditions for compressible viscous flow are difficult to specify, especially when large disturbances are considered. The use of an

additional buffer domain in the vicinity of the wave-tank boundary is indispensable, in particular for subsonic flow, to efficiently dampen wave reflections from the outflow boundary. In this study, the spatially evolving boundary layer over a flat plate is evaluated. The focus in this work is to improve the outflow boundary treatment by adding a buffer domain in the vicinity of the outflow boundary, in which the disturbances are strongly reduced and the flow is gradually brought back to the laminar base flow.

Presentation Outline

In this method, the free surface flows are modeled as immiscible air-water two-phase flows and the free surface itself is represented by the zero level-set function. Calculations were performed for two-dimensional problems like bichromatic wave and beach-breaking flow problems involving violent free surface motions. The level-set RANS method was then employed for simulating the breaking wave on a sloping beach. The numerical results clearly demonstrated the capability of the level-set method to deal with complex free-surface flows involving breaking waves.

Chapter II introduces the general RANS equation and the level-set function. In this mathematical model, both water and air flows are solved in curvilinear coordinate systems. By formulating the RANS equation with the level-set function in a transformed plane, our mathematical model is capable of dealing with complex flow surfaces and configurations.

Chapter III describes the numerical scheme for level-set equation and RANS equations. The third-order TVD scheme and fifth-order WENO scheme are used to discretize the level-set equation.

Chapter IV validates the numerical model by systematic tests on the damping function, grid density and scheme order.

Chapter V presents the performance of this model on bichromatic wave trains and breaking waves on a sloping beach. The properties of breaking points for different cases are described in detail. A comparison of different cases matches the simulation results provided by Garzon and Sethian (2006).

Chapter VI presents the summary and conclusions.

CHAPTER II

GOVERNING EQUATIONS

Introduction

This chapter introduces the general equation Reynolds-Averaged Navier-Stokes (RANS) and level-set function. In this mathematical model, both water and air flows are solved in curvilinear coordinate system. By formulating RANS with level-set function in transformed plane, our mathematical model is convenient to deal with complex flow surface and configurations.

Level-Set Method

Level-set method is widely used for capturing interface evolution. The underlying idea behind level-set methods is to embed an interface Γ in R^3 which bounds an open region $\Omega \subset R^3$ as the zero level-set of a higher dimensional function $\phi(\vec{x},t)$. (Enright et al., 2002).

For air-water two phase flow, the level-set function ϕ has the following properties,

$$\begin{cases} \phi(\vec{x},t) > 0 & \text{for } \vec{x} \in \Omega \\ \phi(\vec{x},t) \le 0 & \text{for } \vec{x} \notin \Omega \end{cases} \tag{1}$$

which means $\phi < 0$ in air region, $\phi > 0$ in water region, and $\phi = 0$ on the air-water interface. We maintain the level-set function as a smooth distance function allowing us to give the interface a thickness fixed in time. Density and surface tension both depend on the level-set function being a distance function.

In the beginning of the calculation, the value of ϕ is the physical distance from the interface. It varies smoothly across the interface and is advected by the local velocity field which is externally given using the advection equation

$$\frac{\partial \phi}{\partial t} + \vec{V} \cdot \nabla \phi = 0 \tag{2}$$

∇ is the gradient operator and $\vec{V} \cdot \nabla \phi = u\phi_x + v\phi_y + w\phi_z$

The interface can be captured at any time by locating the zero level-set. In general, the computed ϕ may not remain the signed distance from the interface and needs to be reinitialized for every time step. Sussman et al. (1994) proposed that this be done by solving the following equation until the steady state is reached:

$$\frac{\partial \phi}{\partial \tau} = sign(\phi_0) \cdot (1 - |\nabla \phi|) \tag{3}$$

where $sign(\phi_0)$ is a one-dimensional smeared out signum function approximated numerically as:

$$sign(\phi_0) = \frac{\phi_0}{\sqrt{\phi_0^{\,2} + (\Delta x)^2}} \tag{4}$$

The advantage of the level-set method is that one can perform numerical computations involving curves and surfaces on an Eulerian approach (with a fixed Cartesian grid). Also, the level-set method makes it easier to follow shapes with changed topology.

In order to void the solution dissolution, a transition zone nearby the zero level-set is built. The transition zone is defined by $|\phi| < \varepsilon$, which is half the thickness of the

interface. In the relative thick transition zone, some fluid properties should be smoothed by the Heaviside function $H(\phi)$: (Sethian, 2001)

$$H(\phi)=\begin{cases}0 & if\ \phi<-\varepsilon\\ \frac{1}{2}[1+\frac{\phi}{\varepsilon}+\frac{1}{\pi}\sin(\frac{\pi\phi}{\varepsilon})] & if\ -\varepsilon\le\phi\le\varepsilon\\ 1 & if\ \phi>\varepsilon\end{cases} \tag{5}$$

ε is a prescribed small number, which is set to be $2\times\Delta x$.

Thus, some fluid properties including density and viscosity will be smoothed in this way:

$$\begin{cases}\rho(\phi)=\rho_a+(\rho_w-\rho_a)\cdot H(\phi)\\ \mu(\phi)=\mu_a+(\mu_w-\mu_a)\cdot H(\phi)\end{cases} \tag{6}$$

In our algorithm, the front must have a uniform thickness; consequently, we must have $|\nabla\phi|=1$ when $|\phi|<\varepsilon$. A function that has this property is a signed distance function near the front. Although we can initialize ϕ in this way, it could not remain the same feature automatically under the evolution of Equation 2.7. Therefore, ϕ must be reinitialized every time step to remain a distance function near the front as the computation proceeds. Re-initialization algorithms maintain the signed distance property by solving the following equation to steady state:

$$\frac{\partial\phi}{\partial\tau}=sign(\phi_0)\cdot(1-|\nabla\phi|) \tag{7}$$

$$sign(\phi_0)=\frac{\phi_0}{\sqrt{\phi_0^{\,2}+(\Delta x)^2}}$$

τ is fractious time, and Δx is grid size.

This guarantees that ϕ has the same sign with zero level-set ϕ_0 and satisfies the condition that $|\nabla\phi| = 1$. Further details could be referred to Sussman et al. (1994, 1998, 1999). The level-set method was shown to be effective in handling topological merging, breaking and self-intersecting of interfaces typically encountered in violent free surface motion problems.

RANS Equations

The Navier-Stokes equations are rewritten in the level-set formulation. Both density and surface tension depend on an assumption point that the level-set function is a function of distance. The fluid properties are assumed to vary smoothly across a narrow transition zone around the free surface. This enables us to obtain accurate and stable numerical results for violent free surface motions encountered in the simulation of breaking wave on sloping beach.

It is assumed that both water and air are governed by the incompressible Navier-Stokes equations (Sussman et al., 1998):

$$\begin{cases} \rho_w(\dfrac{\partial \vec{V}'}{\partial t'} + \vec{V}' \cdot \nabla \vec{V}') = \rho_w \vec{g} + \vec{\mu_w} \nabla^2 \vec{V}' - \nabla p' \\ \rho_a(\dfrac{\partial \vec{V}'}{\partial t'} + \vec{V}' \cdot \nabla \vec{V}') = \rho_a \vec{g} + \vec{\mu_a} \nabla^2 \vec{V}' - \nabla p' \end{cases} \tag{8}$$

$\vec{V}, t, p$ are normalized velocity, time and pressure. They are normalized using the following three dimensionless variables:

$$\vec{V} = \frac{\vec{V}'}{U_0}, t = \frac{t'}{t_0} = \frac{U_0}{L} t', p = \frac{p'}{\rho_w U_0^2} \tag{9}$$

In addition, the non-dimensional density $\rho(\phi)$ and non-dimensional viscosity $\nu(\phi) = \mu(\phi) / \rho(\phi)$ can be represented as below:

$$\begin{cases} \rho(\phi) = \dfrac{\rho}{\rho_w} + (1 - \dfrac{\rho}{\rho_w}) \cdot H(\phi) \\ \mu(\phi) = \dfrac{\mu}{\mu_w} + (1 - \dfrac{\mu}{\mu_w}) \cdot H(\phi) \end{cases} \tag{10}$$

After dividing by $\rho_w U_0^{\,2} / L$ and combining those two equations together, the general Navier-Stokes equations will be:

$$\frac{\partial \vec{V}}{\partial t} + \vec{V} \cdot \nabla \vec{V} = -\frac{\delta_{i,3}}{Fr^2} + \frac{\nu(\phi)}{\mathrm{Re}} \nabla^2 \vec{V} - \frac{1}{\rho(\phi)} \nabla p \tag{11}$$

where Froude number $Fr^2 = \dfrac{U_0^{\,2}}{gL}$ and Reynolds number $\mathrm{Re} = \dfrac{\rho_w U_0 L}{\mu_w}$.

The Navier-Stokes equations for two-fluid flows were written in similar form by Unverdi & Tryggvason (1992). The form of the surface tension we use here is developed by Brackbill et al. (1992) and Chang et al. (1996).

In curvilinear coordinate, the continuity and momentum equations will be (Chen et al. 1990 and Pontaza et al. 2005):

$$\begin{cases} \displaystyle\sum_{i=1}^{3} \frac{\partial U_i}{\partial x^i} = 0 \\ \dfrac{\partial U_i}{\partial t} + \displaystyle\sum_{i=1}^{3} (U_j \frac{\partial U_i}{\partial x^j} + \frac{\partial \overline{u_i u_j}}{\partial x^j}) + \frac{1}{\rho(\phi)} \frac{\partial p}{\partial x^i} - \frac{\nu(\phi)}{\mathrm{Re}} \nabla^2 U_i + \frac{\delta_{i,3}}{Fr^2} = 0 \end{cases} \tag{12}$$

where $\nabla^2 = \displaystyle\sum_{i=1}^{3} \frac{\partial^2}{\partial x^j \partial x^j}$.

The Reynolds stress $\overline{u_i u_j}$ is related to the corresponding mean rate of strain through an isotropic eddy viscosity ν_t:

$$-\overline{u_i u_j} = \nu_t \left(\frac{\partial U_i}{\partial x^j} + \frac{\partial U_j}{\partial x^i}\right) - \frac{2}{3}\delta_{ij} k \tag{13}$$

where $k = (\overline{uu} + \overline{vv} + \overline{ww})/2$ is he turbulent kinetic energy and δ_{ij} is the Kronecker delta. The substitution of Reynolds stress into the momentum equations yields:

$$\frac{\partial U_i}{\partial t} + \sum_{i=1}^{3}\left[\left(U_i - \frac{\partial \nu_t}{\partial x^j}\right)\frac{\partial U_i}{\partial x^j} - \frac{\partial \nu_t}{\partial x^j}\frac{\partial U_j}{\partial x^i}\right] = -\frac{\delta_{i,3}}{Fr^2} + \left(\frac{\nu(\phi)}{\mathrm{Re}} + \nu_t\right)\nabla^2 U_i - \left(\frac{1}{\rho(\phi)}\frac{\partial p}{\partial x^i} + \frac{\partial(\frac{2}{3}k)}{\partial x^i}\right) \tag{14}$$

Let $\varphi = U_i$ and rearrange the momentum equations as follows:

$$\nabla^2 \varphi = R_\varphi \cdot \left[\sum_{i=1}^{3}\left(U_j - \frac{\partial \nu_t}{\partial x^j}\right)\frac{\partial \varphi}{\partial x^j} + \frac{\partial \varphi}{\partial t}\right] + s_\varphi \tag{15}$$

where the effective viscosity is $R_\varphi = \left(\frac{\nu(\phi)}{\mathrm{Re}} + \nu_t\right)^{-1}$ and the source terms are given by:

$$s_\varphi = R_\varphi\left[\frac{1}{\rho(\phi)}\frac{\partial p}{\partial x^i} + \frac{\partial(\frac{2}{3}k)}{\partial x^i} - \sum_{i=1}^{3}\frac{\partial \nu_t}{\partial x^j}\frac{\partial U_j}{\partial x^i} + \frac{\delta_{i,3}}{Fr^2}\right] \tag{16}$$

In the curvilinear coordinate system, those terms can be rewritten in the transformed plane as follows (Chen et al. 1990):

$$\begin{cases} \nabla^2\varphi = \sum_i \sum_j g^{ij} \dfrac{\partial^2 \varphi}{\partial \xi^i \partial \xi^j} + \sum_j f^j \dfrac{\partial \varphi}{\partial \xi^j} \\ \dfrac{\partial \varphi}{\partial t} = \dfrac{\partial \varphi}{\partial \tau} - \dfrac{1}{J} \sum_i \sum_j b_i^{\ j} \dfrac{\partial x^i}{\partial \tau} \dfrac{\partial \varphi}{\partial \xi^j} \\ \sum_j U_j \dfrac{\partial \varphi}{\partial x^j} = \sum_i U_i (\dfrac{1}{J} \sum_j b_i^{\ j} \dfrac{\partial \varphi}{\partial \xi_j}) \\ -\dfrac{\partial \nu_t}{\partial x^j} \dfrac{\partial \varphi}{\partial x^j} = -\sum_n [\dfrac{1}{J} \sum_m b_n^{\ m} \dfrac{\partial \nu_t}{\partial \xi^m} \cdot \dfrac{1}{J} \sum_j b_n^{\ j} \dfrac{\partial \varphi}{\partial \xi^j}] \end{cases} \tag{17}$$

Here, $b_i^{\ j}, g^{ij}, f^j$ and the Jacobian J are geometric coefficients in the curvilinear coordinate system whose values can be readily evaluated in the transformed plane. When we plug these terms into equation, we can get:

$$\sum_i \sum_j g^{ij} \frac{\partial^2 \varphi}{\partial \xi^i \partial \xi^j} - \sum_j 2a_\varphi^{\ j} \frac{\partial \varphi}{\partial \xi^j} = R_\varphi \frac{\partial \varphi}{\partial \tau} + s_\varphi \tag{18}$$

where, $2a_\varphi^{\ j} = \dfrac{R_\varphi}{J} \sum_n b_n^{\ j} [U_n - \dfrac{\partial x_i}{\partial \tau} - \sum_m \dfrac{1}{J} b_n^{\ m} \dfrac{\partial \nu_t}{\partial \xi^m}] - f^i$

Note that:

$$\sum_i \sum_j g^{ij} \frac{\partial^2 \varphi}{\partial \xi^i \partial \xi^j} = g^{11} \frac{\partial^2 \varphi}{\partial \xi^1 \partial \xi^1} + g^{22} \frac{\partial^2 \varphi}{\partial \xi^2 \partial \xi^2} + g^{33} \frac{\partial^2 \varphi}{\partial \xi^3 \partial \xi^3} + 2(g^{12} \frac{\partial^2 \varphi}{\partial \xi^1 \partial \xi^2} + g^{23} \frac{\partial^2 \varphi}{\partial \xi^2 \partial \xi^3} + g^{31} \frac{\partial^2 \varphi}{\partial \xi^3 \partial \xi^1}) \tag{19}$$

Plug Eq. (19) into Eq. (18), we will get:

$$\sum_j (g^{jj} \frac{\partial^2 \varphi}{\partial \xi^j \partial \xi^j} - 2a_\varphi^{\ j} \frac{\partial \varphi}{\partial \xi^j}) = R_\varphi \frac{\partial \varphi}{\partial \tau} + S_\varphi \tag{20}$$

$$S_\varphi = s_\varphi - 2(g^{12} \frac{\partial^2 \varphi}{\partial \xi^1 \partial \xi^2} + g^{23} \frac{\partial^2 \varphi}{\partial \xi^2 \partial \xi^3} + g^{31} \frac{\partial^2 \varphi}{\partial \xi^3 \partial \xi^1}) \tag{21}$$

The momentum equation and the continuity equation are the Reynolds-Averaged Navier-Stokes (RANS) equation for unsteady, three-dimensional turbulent flows.

Velocity Extrapolation

While the Navier-Stokes equations can be used to obtain velocities for the liquid volume and air field, the complex water surface like wave over turning would produce a big difference for water and air velocities. The solution will diverge if the neighboring values have a huge difference. The one-way extrapolation formula introduced by Stanley Osher (2003) is applied.

When applying level-set function to update water surface, the velocity would be affected a lot by the air field, which could be a large value in opposite direction to the water velocity. Usually velocity extrapolation is needed for one side (i.e. $\phi < 0$, side of the free surface). Since these velocity conditions were used not only to update the velocity but to evolve the level-set, we need velocity extrapolation in a few grid cells deep into the $\phi < 0$, region. Thus, we take an approach using constant extrapolation of the liquid velocities from inside the liquid in the direction normal to the interface.

The velocity extrapolation equation is:

$$\frac{\partial \vec{u}_{ext}}{\partial \tau} + \vec{N} \cdot \nabla \vec{u}_{ext} = 0 \tag{22}$$

$$\vec{N} = \frac{\nabla \phi}{|\nabla \phi|} \tag{23}$$

where τ is a fictitious time. At steady state we note that $\nabla \phi \times \nabla \vec{u}_{ext} = 0$. We usually populate a 3 to 5 grid cell band in the $\phi<0$ region with extension velocities. Note that as

the grid resolution approaches zero, these extension velocities do indeed solve the $\nabla u = 0$ condition.

In curvilinear coordinate:

$$|\nabla\phi| = \sqrt{\nabla\phi\cdot\nabla\phi} = \sqrt{\phi_{,i}\phi_{,j}\vec{a}^{i}\vec{a}^{j}} = \sqrt{g^{ij}\phi_{,i}\phi_{,j}}$$

$$\vec{N} = \frac{\phi_{\xi}}{|\phi|}\vec{a}^{1} + \frac{\phi_{\eta}}{|\phi|}\vec{a}^{2} + \frac{\phi_{\zeta}}{|\phi|}\vec{a}^{3} = N_i\vec{a}^{i}, N_i = \frac{\phi_{,i}}{|\nabla\phi|} \tag{24}$$

$$\frac{\partial\vec{u}_{ext}}{\partial\tau} + \vec{N}\cdot\nabla\vec{u}_{ext} = \frac{\partial\vec{u}_{ext}}{\partial\tau} + \frac{g^{ij}\phi_{,i}u_{ext,j}}{g^{mn}\phi_{,m}\phi_{,n}} = 0 \tag{25}$$

CHAPTER III

NUMERICAL EQUATION

The level-set evolution equation is written in (ξ,η) coordinates as:

$$\frac{\partial \phi}{\partial t}+\sum_{i=1}^{3}\frac{\partial (U^{i}\phi)}{\partial \xi^{i}}=0 \tag{26}$$

The contravariant velocity components (Chen and Patel, 1989):

$$U^{i}=JV^{i}=\sum_{j=1}^{3}b_{j}^{i}U_{j} \tag{27}$$

In the present study, the equation is advanced using the 3rd-order TVD Runge-Kutta scheme which is total variation stable (Yue et al., 2003).

$$\begin{cases}\phi^{(1)}=\phi^{n}-\Delta t\cdot R(\phi^{n})\\ \phi^{(2)}=\frac{3}{4}\phi^{(n)}+\frac{1}{4}\phi^{(1)}-\frac{\Delta t}{4}R(\phi^{(1)})\\ \phi^{(n+1)}=\frac{1}{3}\phi^{(n)}+\frac{2}{3}\phi^{(2)}-\frac{2\Delta t}{3}R(\phi^{(2)})\end{cases} \tag{28}$$

where $R(\phi)=\partial(U^{i}\phi)/\partial\xi^{i}$ and the spatial operator R is discretized in transformed plane (ξ,η,ζ) in a conservative manner.

$$\frac{\partial (U^{i}\phi)}{\partial \xi^{i}}=(U^{1}\phi)_{i+1/2,j,k}-(U^{1}\phi)_{i-1/2,j,k}+(U^{2}\phi)_{i,j+1/2,k}-(U^{2}\phi)_{i,j-1/2,k}+(U^{3}\phi)_{i,j,k+1/2}-(U^{3}\phi)_{i,j,k-1/2} \tag{29}$$

To disctritize the spatial term, the fifth order WENO scheme in curvilinear coordinate is used:

$$\phi_{\xi} = \omega_1 \phi_{\xi}^{\ 1} + \omega_2 \phi_{\xi}^{\ 2} + \omega_3 \phi_{\xi}^{\ 3} \tag{30}$$

where $\omega_k \in (0,1)$ and $\omega_1 + \omega_2 + \omega_3 = 1$.

Jiang, Shu (1996) and Jiang and Peng (2000) have made study on the weight parameters to keep HJ WENO to $O((\Delta\xi)^5)$ in smooth regions. They define the weights ω_k as follows:

$$\begin{aligned} \omega_1 &= \frac{\alpha_1}{\alpha_1 + \alpha_2 + \alpha_3} \\ \omega_2 &= \frac{\alpha_2}{\alpha_1 + \alpha_2 + \alpha_3} \\ \omega_3 &= \frac{\alpha_3}{\alpha_1 + \alpha_2 + \alpha_3} \end{aligned} \tag{31}$$

$$\begin{aligned} \alpha_1 &= \frac{0.1}{(S_1 + \varepsilon)^2} \\ \alpha_2 &= \frac{0.6}{(S_2 + \varepsilon)^2} \\ \alpha_3 &= \frac{0.3}{(S_3 + \varepsilon)^2} \end{aligned} \tag{32}$$

with $\varepsilon = 10^{-6}$:

$$\begin{aligned} S_1 &= \frac{13}{12}(v_1 - 2v_2 + v_3)^2 + \frac{1}{4}(v_1 - 4v_2 + 3v_3)^2 \\ S_2 &= \frac{13}{12}(v_2 - 2v_3 + v_4)^2 + \frac{1}{4}(v_2 - 4v_4)^2 \\ S_3 &= \frac{13}{12}(v_3 - 2v_4 + v_5)^2 + \frac{1}{4}(3v_3 - 4v_4 + v_5)^2 \end{aligned} \tag{33}$$

$$\upsilon_1 = D^- \phi_{i-2}, \upsilon_2 = D^- \phi_{I-1}, \upsilon_3 = D^- \phi_i, \upsilon_4 = D^- \phi_{i+1}, \upsilon_5 = D^- \phi_{i+2} \quad (34)$$

$$D^- \phi_i = \frac{\phi_i - \phi_{i-1}}{\Delta \xi} \quad (35)$$

In smooth region, three weight coefficients are equally significant and produce 5th order accuracy. In the non-smooth region, the combination of weight coefficient values would make the WENO back to 3rd order ENO, which is $O((\Delta \xi)^3)$.

CHAPTER IV

VERIFICATION OF PRESENT MODEL

The level-set FANS method was employed recently by Chen and Yu (2006) and Yu et al. (2007) for time-domain simulations of greenwater on 2D offshore platforms and 3D sloshing flows in a liquefied natural gas (LNG) tank. In the present study, fifth-order WENO scheme was incorporated into their previous work to get higher accuracy solution. It is tested for monochromatic wave, bichromatic wave and more complex free surface including breaking wave.

Zalesak's Problem

The Zalesak's two-dimensional problem (Zalesak, 1978) is a common test for the quality of an advection scheme. This problem consists of a slotted solid disk rotating in a 100 × 100 square domain. The solid area is a cut out circle of radius R = 15 (normalized by the unit grid size), advected by a counterclockwise rotating flow field with constant angular velocity Ω (Figure 1). The diameter of the circle is 30, and the slot width is d = 6 as shown in Figure 2. The slotted solid disk is initially centered at (50, 75) and rotates around a center (50, 50). The velocity field is given by

$$\begin{aligned} u_0 &= \Omega \times (50 - y) \\ v_0 &= \Omega \times (x - 50) \\ \phi_0 &= \text{ signed distance from object} \end{aligned} \tag{36}$$

The computational grid contains 100×100 regular square elements so that the mesh size is $\Delta x = \Delta y = 1$ as shown in Figure 3.

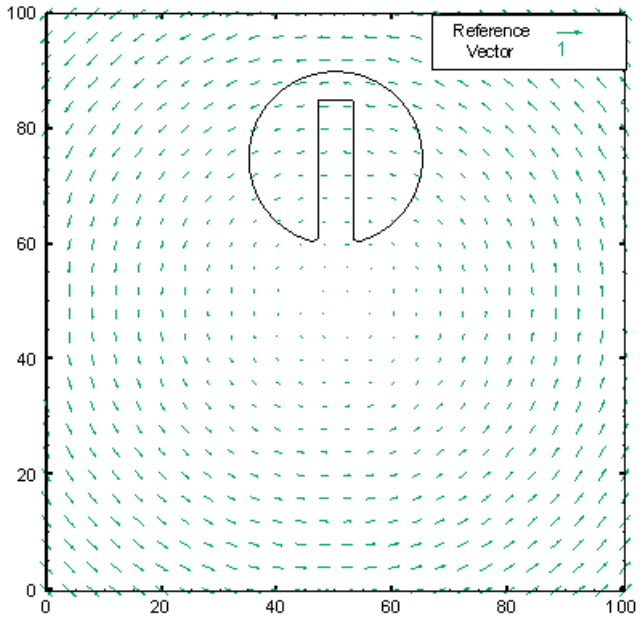

Figure 1 Zalesak's Problem: velocity field

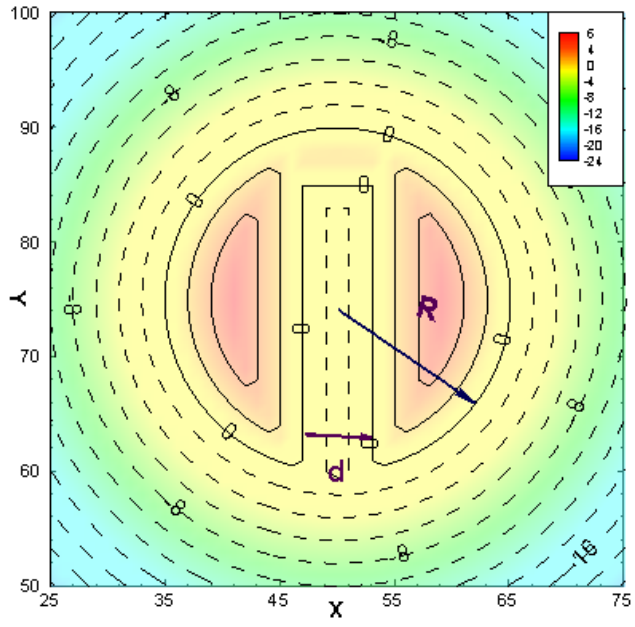

Figure 2 Zalesak's Problem: initial position and contour plot of ϕ

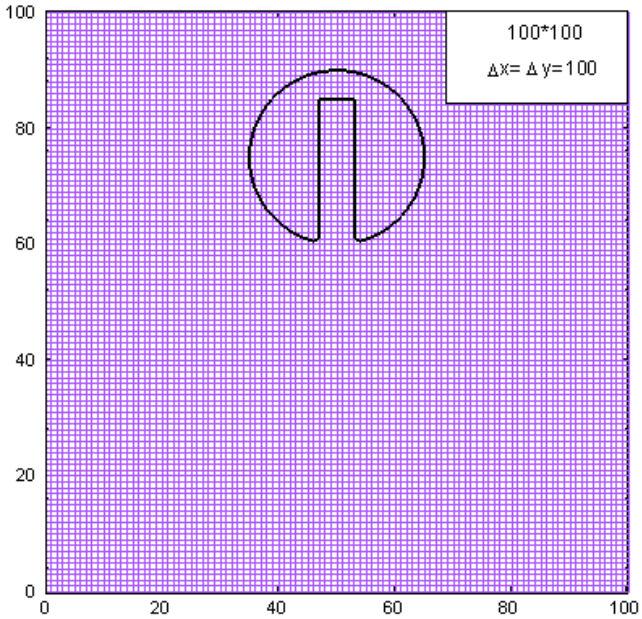

Figure 3 Zalesak's Problem: uniform grid in domain 100*100.

Two simulations were performed: one with the third-order TVD Runge-Kutta scheme in time coupled with the third-order Hamiliton-Jacobi essentially non-oscillatory (HJENO) (Osher and Fedkiw, 2003) function in space; and the other with the same third-order TVD Runge-Kutta scheme in time, but coupled with fifth-order WENO scheme (Liu, Osher and Chan,1994) in space. In each case, the time step Δt was set to 0.01 s, and 628 time iterations were needed for the disk to perform one complete cycle. Figure 3 shows the numerical grids and the slotted disk edges (solid lines) at time step = 0, 157, 314, 471, and 628. The dotted line in Figure 4 represents the initial geometry of the disk. The dashed line in Figure 4 is the disk geometry imposing the third-order HJENO scheme at time step = 628, while the solid line denotes the computed slotted disk edges using the WENO scheme. For both cases, one can readily see that the shape of the cut

out circle remains unchanged except at the corners, which are slightly rounded because of the small numerical diffusion. From comparison, a higher order scheme such as the WENO scheme is much more accurate at the corners compared to the ENO scheme. Also, this error accumulates with increasing computing time. This clearly shows the efficiency of the WENO scheme compared to the third-order HJENO scheme.

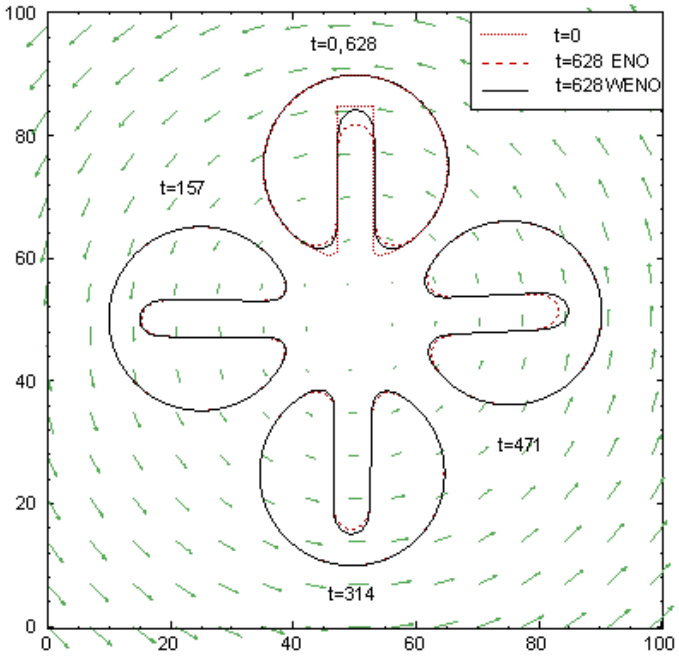

Figure 4 Zalesk's problem: comparison of predicted interfaces at t = 0, 157, 314, 471, and 628, using HJENO and WENO scheme

Monochromic Wave Propagation

In this study, a two-dimensional numerical wave tank in a viscous fluid was used to simulate the propagation of water waves over flat bottoms. Evolution of wave and flow

fields are described and discussed in detail. The still water depth is indicated by H in Figure 5.

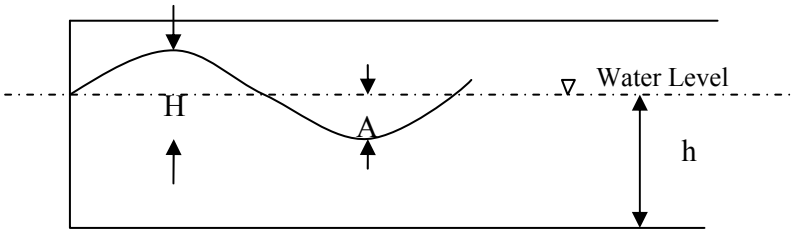

Figure 5: 2D schematic diagram for wave maker

Experimental Setup

Monochromic waves were generated at one end of a two-dimensional wave flume. This wave flume was a two-dimensional nonlinear numerical wave tank based on the chimera RANS method combined with the level-set method. To verify the accuracy of the present numerical scheme, monochromic waves propagating in the entire domain and solved by RANS equations were coupled with applying the level-set method third-order TVD Runge-Kutta scheme (Yue et al. 2003), and the fifth-order WENO scheme (Liu, Osher and Chan 1994) to the discrete level-set equation. The waves downstream were dissipated by imposing numerical dampening on the free surface. The numerical damping was applied on kinematic free-surface conditions.

In the fully nonlinear computation, the length of the damping zone was twice the wavelength. In the longitudinal direction, equally spaced 80 cells in one wavelength were used. In the vertical direction, a variable mesh system with a denser cell distribution near the free surface and its size increasing with depth is employed. Near the free surface, 20 cells were used in the vertical distance H. For the computational domain,

400 elements were distributed on the free surface and 40 elements on the wave maker, which is a half wavelength. The time increment T used for the present computation is T/200. Wave profiles were tested on different cases depending on the damping function and grid density. Also, we compare the result with the third-order HJENO scheme, which was previously completed by Yu (2007).

Buffer Domain Treatments

To prevent reflection of the wave fluctuations that can disturb the wave profile in the wave tank, an artificial buffer domain is needed. An extra zone is attached to the edge of the wave-tank domain. Within this extra zone, the amplitude of the out-going wave is dampened to a set target value.

There are several ways to dampen wave fluctuations, including a considerable increase of the viscosity (Liu, 1994), a gradual change of the governing equations in a parabolic system (Prutte, 1995), and removing the disturbance component from the convective velocity (Prutte, 1995).

Experimentally, it has been shown that the larger the viscosity increase, the more effective is the buffer domain. However, higher viscosity would limit the allowable time step, and this would restrict the entire numerical method. For the parabolic procedure, the buffer domain works slowly and is costly.

In our test, we adopt an efficient method by directly multiplying the disturbances with an appropriate dampening function. This technique gives a better result than from the method that only removes disturbances from the convective velocity, even with a shorter buffer domain (Wasistho, 1997).

To simplify our model, a sinusoidal wave of very small wave steepness, which alters the profile to a linear wave, is superimposed in the wave maker. The input wave has constant frequency and amplitude. Although constant frequency and amplitude do not make physical sense, it is a good approximation to a nonlinear wave when the wave steepness is small. After the wave propagates, the wave shape changes with the crests becoming more sharply peaked and the troughs shallower and flatter after only a few time periods. The wave then maintains a relatively steady profile and continues to propagate until it reaches the buffer zone where the amplitude is gradually reduced by multiplying the distributions of velocities with a damping function. Usually the damping function decreases from 1 to 0, which reduces the wave profile to a reference value. This approach could be described by the following formula (Wasistho, 1997):

$$\mathrm{U} = \mathrm{U}_{ref} + \zeta(x_l)(\hat{U} - U_{ref}) \tag{37}$$

where $U = (u_i, p)^T$, U_{ref} is the referenced solution and $\hat{U}$ is the solution calculated at each time step without applying the damping function. ς is the damping function.

Wasistho et al. (1997) have compared the damping rates of different types of damping functions according to the buffer zone grid quality, buffer zone domain type, and the input wave property. According to their result, we choose Damping Function 1 as the one which was recommended to effectively reduce wave reflections, and compare it to the one commonly used for damping out the waves as Function 2.

For Function 1, x_s and x_e are the values of x_l at the beginning and the end of the buffer domain. The buffer zone domain coordinates range from 0 to 1 when it moves from the beginning to the end of the buffer zone.

Function 1 is:

$$\zeta = (1 - C_1 x_b^{\,2})\left(1 - \frac{1 - e^{C_2 x_b^{\,2}}}{1 - e^{C_2}}\right) \quad with \quad 0 \le C_1 < 1,\ C_2 > 0. \tag{38}$$

$$x_b = \frac{x_l - x_s}{x_e - x_s} \tag{39}$$

We take C_1=0.005 and C_2=20 during test. x_s and x_e are the values of x_l at the beginning and the end of the buffer domain, then the buffer domain coordinate ranges from 0 to 1 when it moves from the beginning to the end of the buffer zone.

Function 2 is:

$$\zeta = \frac{1 + \cos(x_b \times \pi)}{2} \tag{40}$$

x_b is defined in Eq.39.

For both function expressions, and ζ satisfies the following dampening function constraints:

$$\begin{aligned} &\zeta(0) = 1 \\ &\frac{\partial \zeta}{\partial x_b}(x_b) \le 0 \; if \; x_b > 0 \\ &\frac{\partial \zeta}{\partial x_b}(0) = 0 \\ &\zeta(1) = 0. \end{aligned} \tag{41}$$

Table 1 Locations of wave elevation measurement

Points	Location(m)
P1	2
P2	4
P3	6

As described previously, the length of the entire domain is selected to be six wavelengths, in which the last two are optionally used as a buffer domain. The computational domain size is 1.6 m$\times$12.0 m (Figure 6). If we use a water depth of h = 1 m to normalize the spatial value, the wavelength is a dimensionless value 2.0. The height of the computational domain ranges from -1.0 to 0.6 in the y-direction. The steady water level is at y = 0.0, which is also the reference value. Wave elevation would be measured from three gauges (Table 1). The surface gravity in the wave maker is a sinusoidal function of the form:

$$y(x,t) = A\cos(\frac{2\pi(x-Ct)}{L}) \tag{42}$$

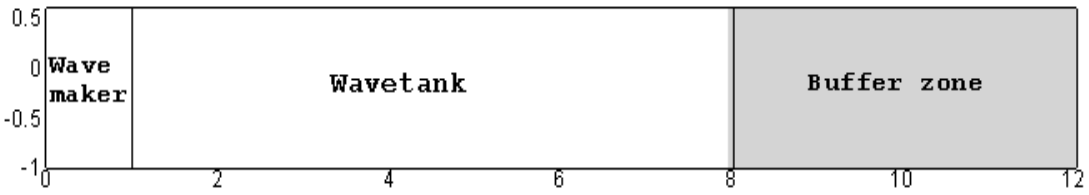

Figure 6 Schematic of buffer zone implementation

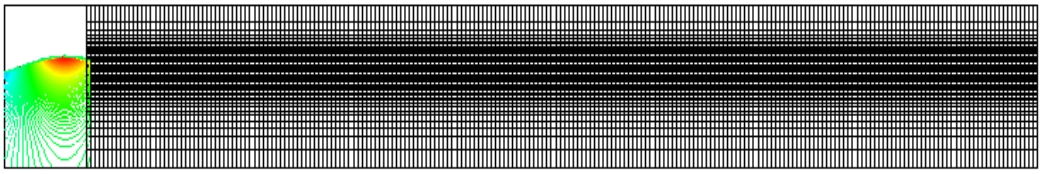

Figure 7 Typical mesh for 2D wave maker (Refine mesh near the free surface)

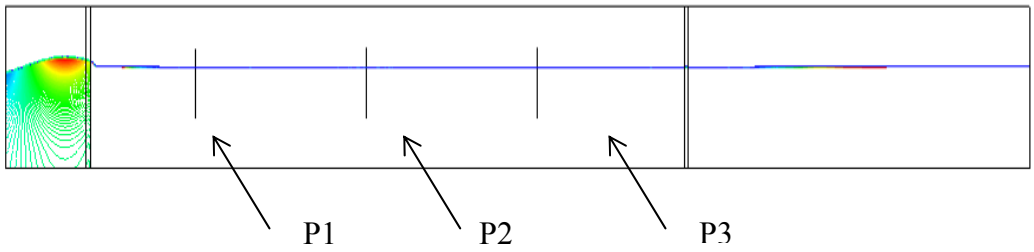

Figure 8 Computational domain for 2D wave maker

Amplitude A equals 0.1 and the wavelength L is 2.0. We use a fifth-order WENO third-order TVD Runge-Kutta scheme and a 400 x 85 grid for our computational domain (Figure 7 and Figure 8). As an illustration, the shapes of five damping functions are depicted in Figure 9. To validate the performance of the damping function, we tested the buffer domain successively and tried to obtain the narrow one that exhibits very small upstream influences. We used the following procedure:

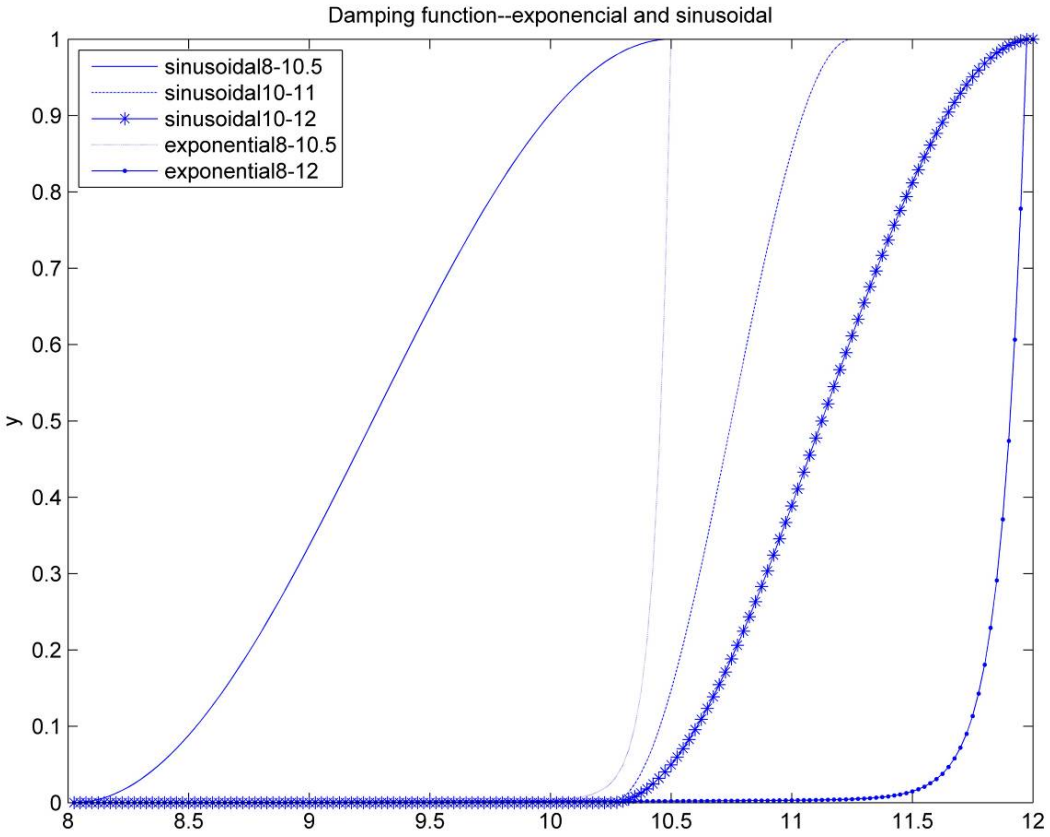

Figure 9 Shape of five damping functions tested within the buffer domain

Test 1: By applying the sinusoidal dampening function on the first 2/3 of the buffer domain where x = (8.0, 10.5), the wave profile and velocity distribution at a specific time is shown in Figure 10. The wave profile along the wave tank, x = 1~8, is shown in time steps on Figure 11.

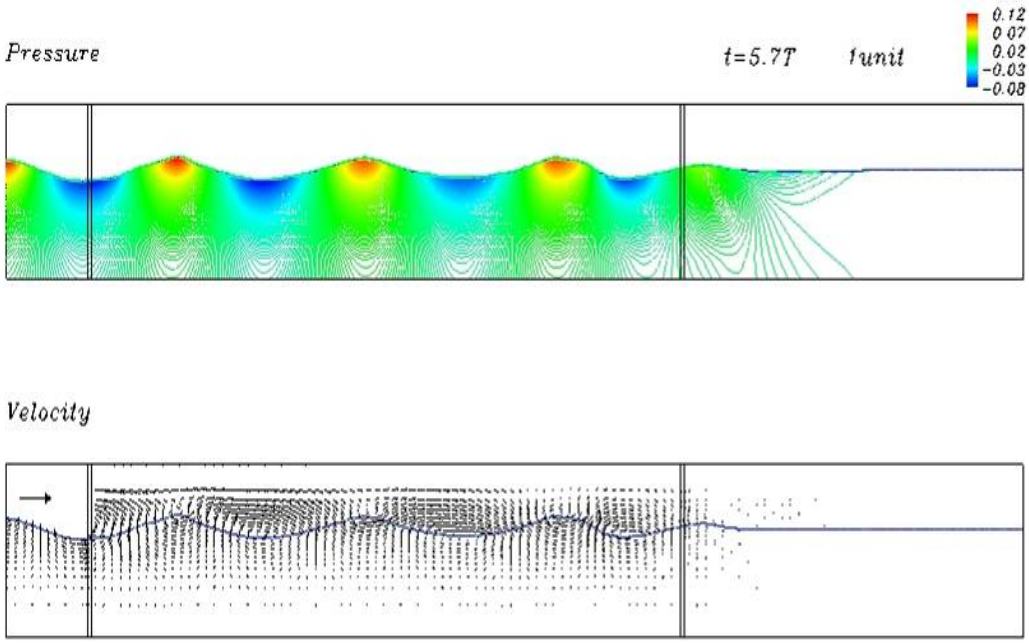

Figure 10 Test 1: Wave profile and velocity distribution at t=5.7T

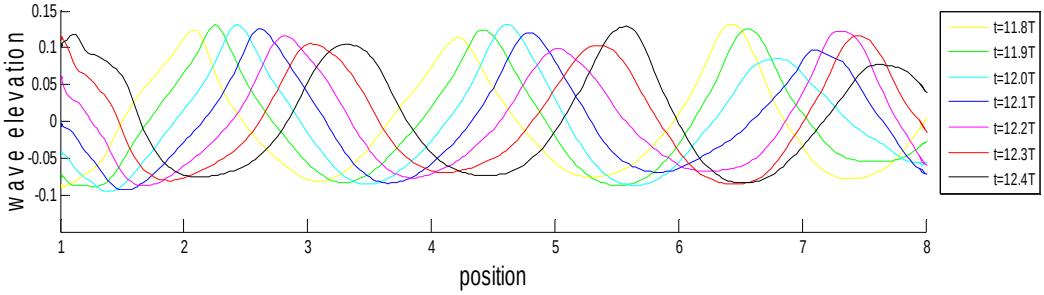

Figure 11 Test 1: Wave profile at consequent time (t=11.8T, 11.9T, 12.0T, 12.1T, 2.2T, 12.3T, and 12.4T)

At time t = 5.7T, the wave is almost damped out in the entire buffer zone. There is no pressure higher than 0.07 and the velocity also decreases very rapidly. From the wave train propagation shown in Figure 11, this damping function has very explicit reflection

wave properties in most of the computation domain. The disturbance is caused by a sudden compression of the amplitude. The reduction of disturbances is carried out in every stage. This accumulative effect makes the reduction of disturbances more rapid than the damping functions. Although the sinusoidal damping function satisfies the four constraints, it gradually changes. The sinusoidal damping function can also produce an abrupt decrease of the disturbance amplitudes and produce reflections in the computational domain.

Test 2: Next, we test the exponential dampening function and apply it at the same buffer zone ranging from 8.0 to 10.5. The pressure, velocity and propagation of the wave train are shown in Figure 12 and Figure 13. Comparing the first two tests, we see that the exponential damping function is slightly improved (Figure 14) compared with Test 1.

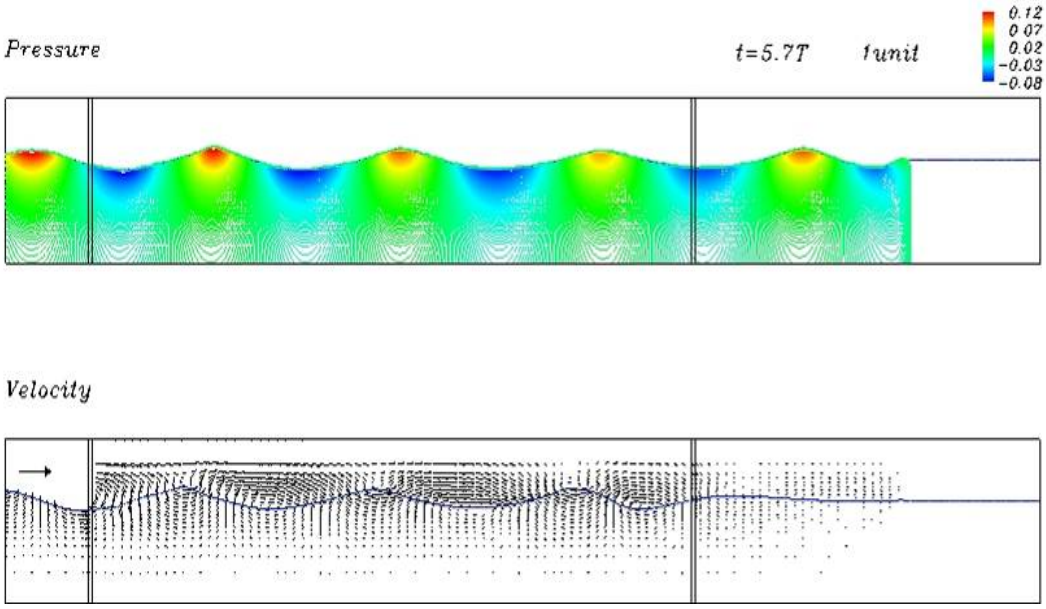

Figure 12 Test 2: Wave profile and velocity distribution at t=5.7T

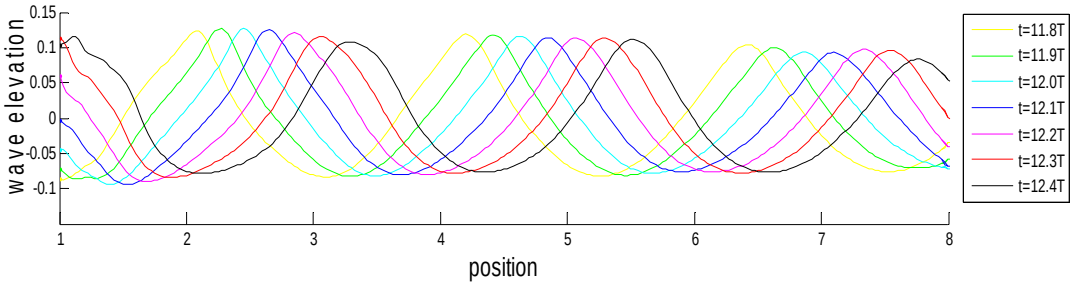

Figure 13 Test 2: Wave profile at consequent time (t=11.8T, 11.9T, 12.0T, 12.1T, 12.2T, 12.3T, and 12.4T)

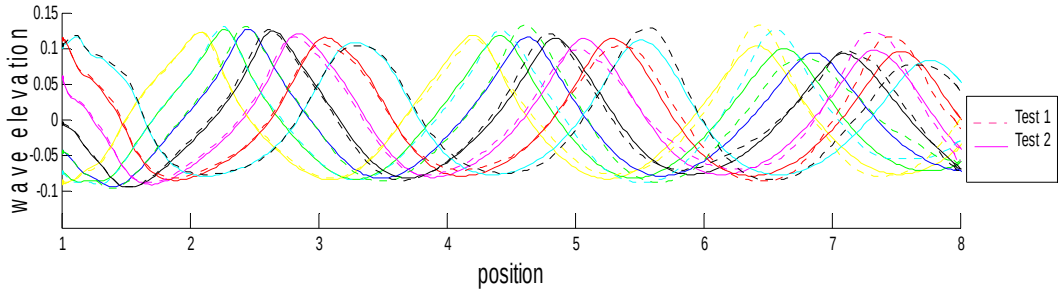

Figure 14 Comparison of Test 1 and Test 2

Compared to the sinusoidal function, this damping function has much better control of the reflected waves, and even the wave shape does not change significantly in the front of the buffer zone. We found that the propagating wave train could be held with sufficient amplitude. A minor problem with this model is that the wave amplitude decreases when propagating, which may be caused by a somewhat coarse grid and the properties of the nonlinear wave itself.

Test 3: To identify the main reason for the reflected waves caused by the sinusoidal damping function, we modified the original sinusoidal damping function to change the shape in a narrow zone and match that of the exponential damping function. We tested

the sinusoidal function by only applying it on (10.3, 10.5) and analyzed the results as shown in Figure 15 and Figure 16.

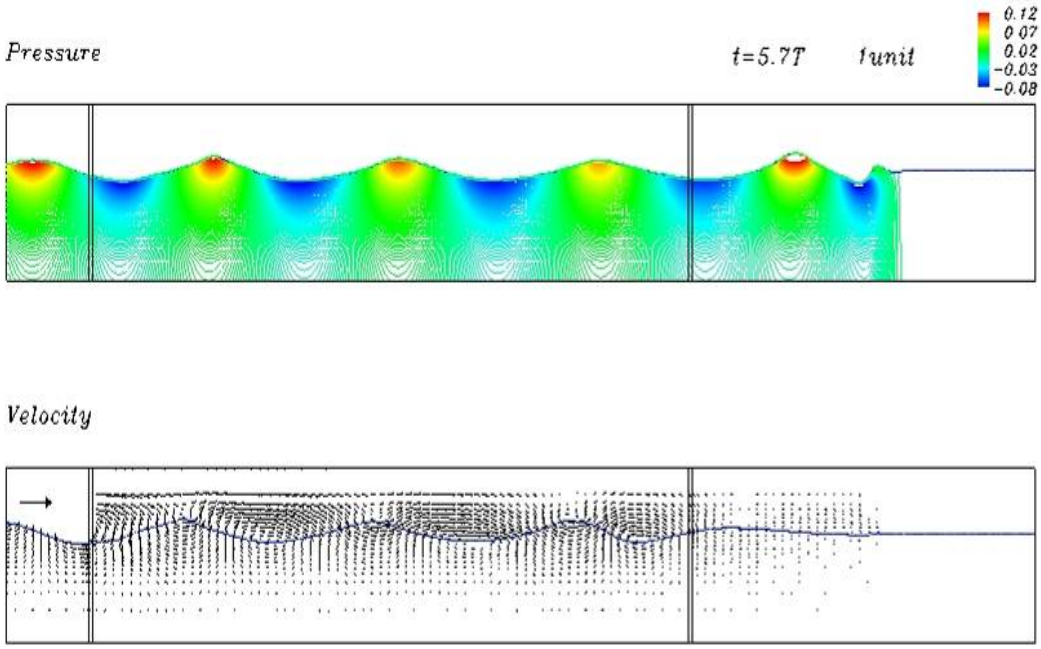

Figure 15 Test 3: Wave profile and velocity distribution at t=5.7T

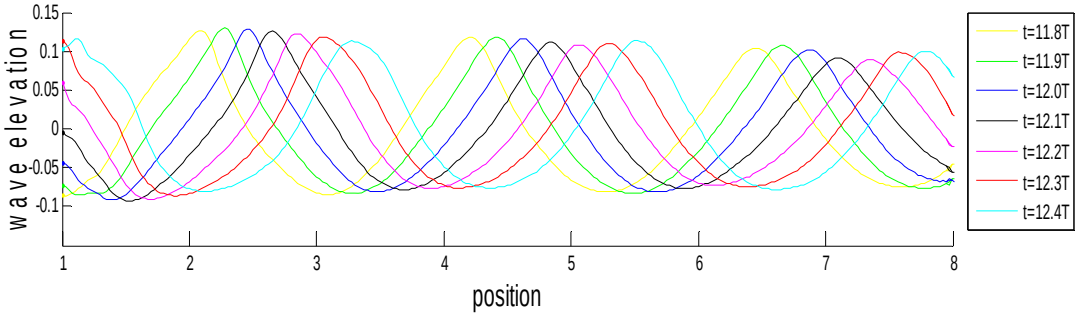

Figure 16 Test 3: Wave profile at consequent time (t=11.8T, 11.9T, 12.0T, 12.1T, 12.2T, 12.3T, and 12.4T)

We could still identify the reflected waves, which are smaller than the sinusoidal dampening function applied from x = 8.0. We conclude that although in such a narrow zone, which is 0.2 in width, the small difference between the sinusoidal and exponential damping functions could result in very obvious effects on the reflection.

Test 4 and 5: Originally, the requirement called for the sinusoidal dampening function to cover a bandwidth no less than half the wavelength. To eliminate the possibility that reflection is caused by a deficient buffer zone width, we extended the sinusoidal damping function and made it cover from 10.2 to 11, which is longer than half the wave length (1.0). The results, in Figure 17 and Figure 18 show that there is actually almost no disturbance. With an increase in the domain, this sinusoidal dampening function covers less change of its value on unit length. The sinusoidal dampening function was extended to the end of entire domain and covered from 10.2 to 12. Figure 19 and Figure 20 show the results for Test 5.

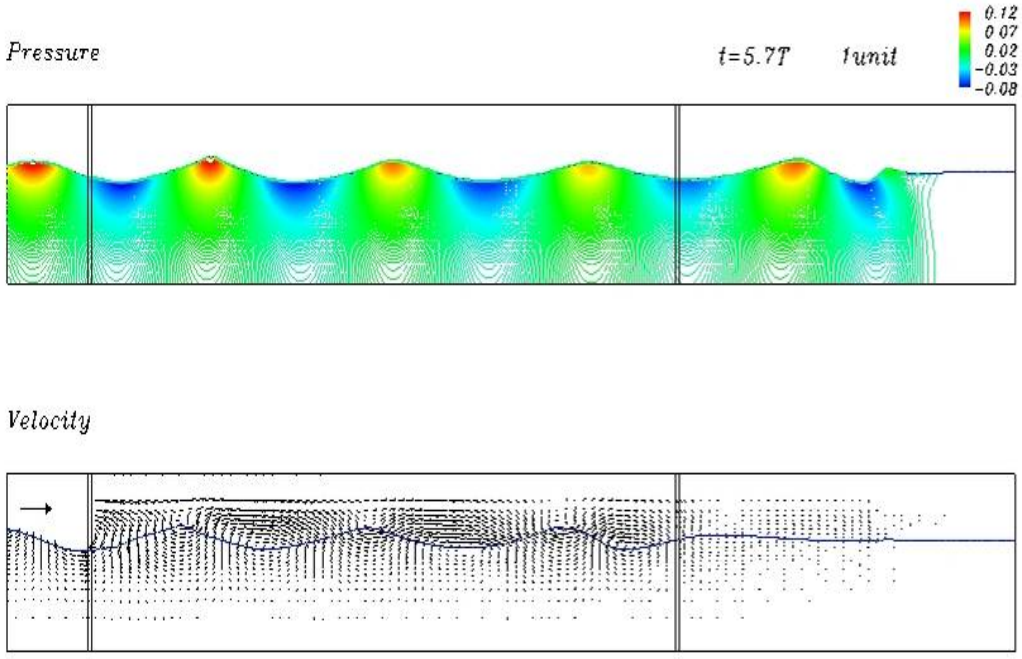

Figure 17 Test 4: Wave profile and velocity distribution at t=5.7T

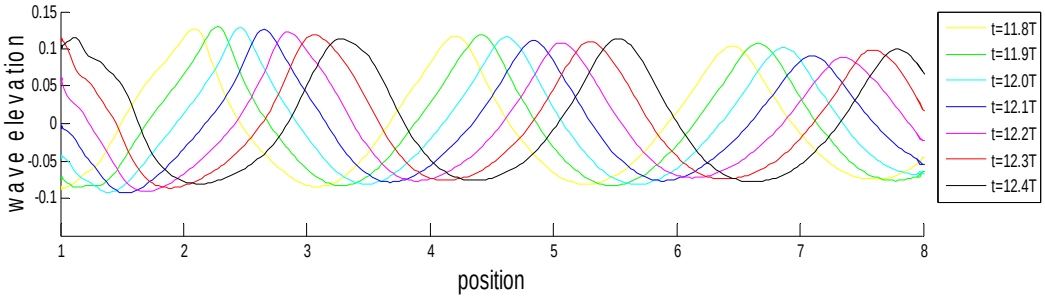

Figure 18 Test 4: Wave profile at consequent time (t=11.8T, 11.9T, 12.0T, 12.1T, 12.2T, 12.3T, and 12.4T)

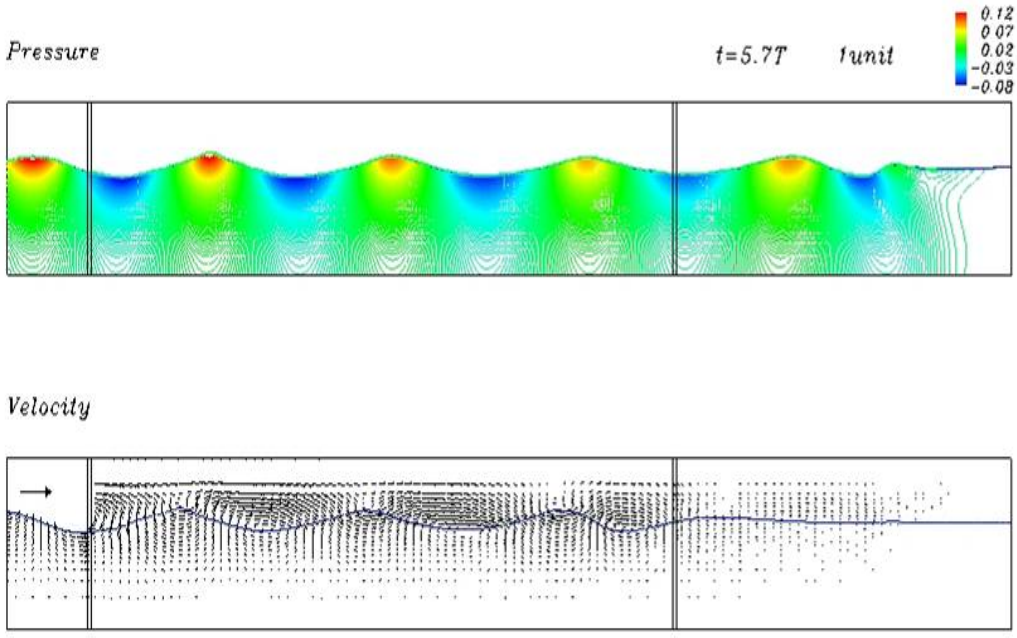

Figure 19 Test 5: Wave profile and velocity distribution at t=5.7T

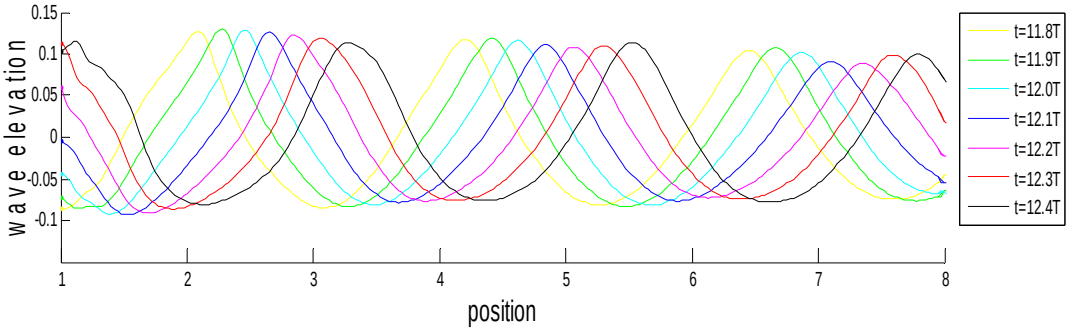

Figure 20 Test 5: Wave profile at consequent time (t=11.8T, 11.9T, 12.0T, 12.1T, 12.2T, 12.3T, and 12.4T)

From Test 1, 3, 4, and 5 we could find that sinusoidal damping function is not an effective approach even when it is applied on longer buffer domain length.

Test 6: To make the entire series of tests more systematic, we also want to analyze the propagating wave train with an exponential function applied on a longer domain. This test could help us find a more effective damping function by narrowing the domain needed for computations. The exponential dampening function was applied on x = (8.0, 12.0), and the results are shown in Figure 21 and Figure 22. A comparison of Test 2 and Test 6 is shown in Figure 23.

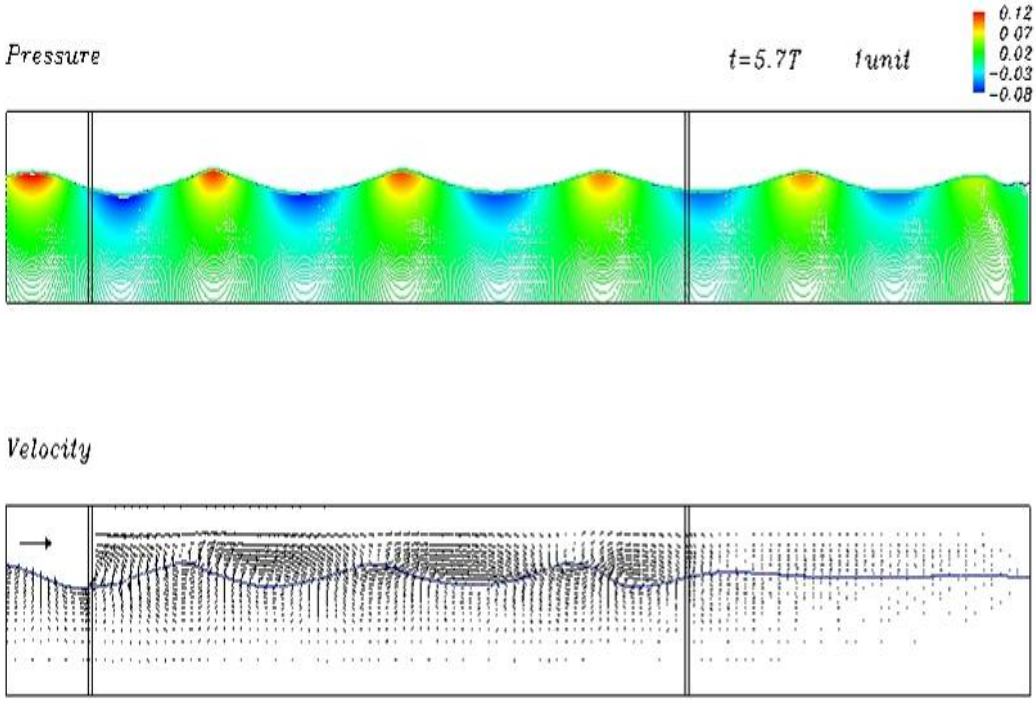

Figure 21 Test 6: Wave profile and velocity distribution at t=5.7T

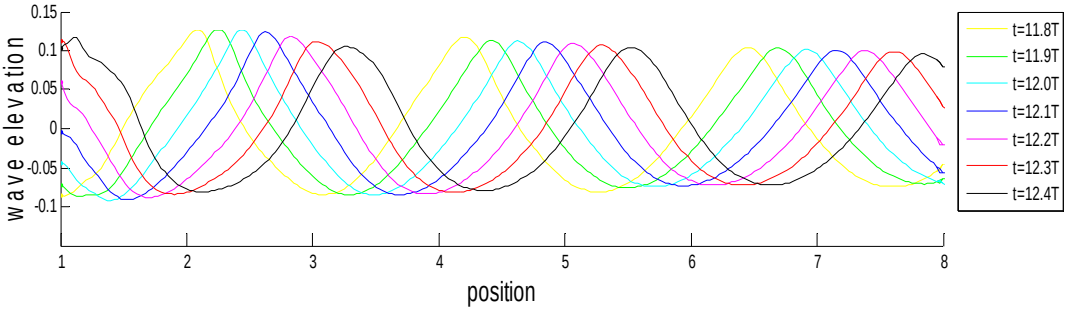

Figure 22 Test 6: Wave profile at consequent time (t=11.8T, 11.9T, 12.0T, 12.1T, 12.2T, 12.3T, and 12.4T)

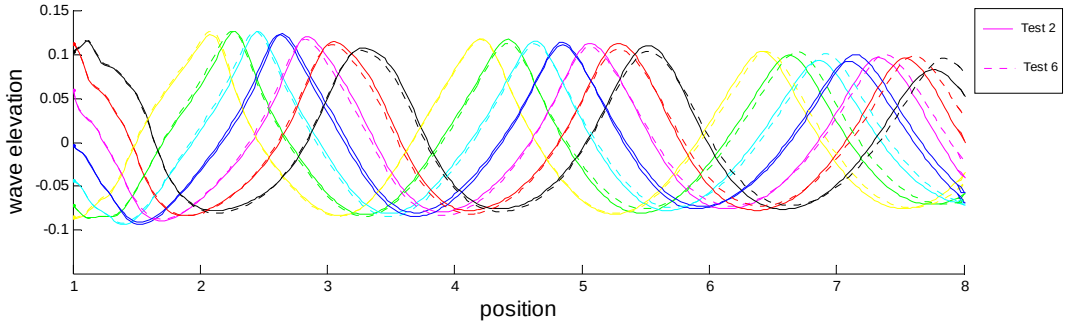

Figure 23 Comparison of Test 2 and Test 6

In the last test, damping function is defined as:

$$\zeta = (1 - C_1 x_b^{\,2})\left(1 - \frac{1 - e^{C_2 x_b^{\,2}}}{1 - e^{C_2}}\right) \quad with \quad 0 \le C_1 < 1,\ C_2 > 0. \tag{43}$$

C1=0.005 and C2= 20

$$x_b = \frac{x_l - x_s}{x_e - x_s}$$

For our uniform grid density model, the numerical tests have shown that the exponential damping function applied over a range from 8.0 to 12.0 is more efficient

than other damping functions. Note that the parameter $C_1 = 0.005$ forces a much more gradual suppression of disturbances in the front part of the bugger domain, and the increased value $C_2 = 20$ postpones a rapid decrease in the disturbance. Based on this result, an effective damping function with very small upstream influences is established and will be used in other numerical models.

Grid Refinement Study

From the numerical tests in Chapter IV, we notice that the wave amplitude decreases when the waves are propagating in the computational domain, even for the most effective damping conditions. Actually, the density of elements in the numerical model plays an important role in obtaining more accurate solutions.

The grid we used is 20 cells in wave height and 80 cells in wave length. The wave profile accuracy has a different sensitivity in wave height and length directions with a 0.2-m height and a 2.0-m length. To achieve a more efficient grid with less cost but higher accuracy, we performed some simple performance tests initially on a coarser grid. Less computation time is needed with the coarser grid while it still maintains the tendency of grid sensitivity in different directions. In studying the base on the grid of the buffer zone, we divided the computational domain into three blocks, exactly the same as the wave maker, wave tank and buffer zone fields (Figure 24). In this way, we were able to keep the wave maker and buffer zones unchanged needing only to refine or reduce the grid in the wave-tank domain to reduce computation costs. The tests we made were based on the grid shown in Table 2.

Table 2 Grid density for Test 1 and Test 2

Simple Tests:	No. of Elements:
Test 1	145*42
Test 2	145*84

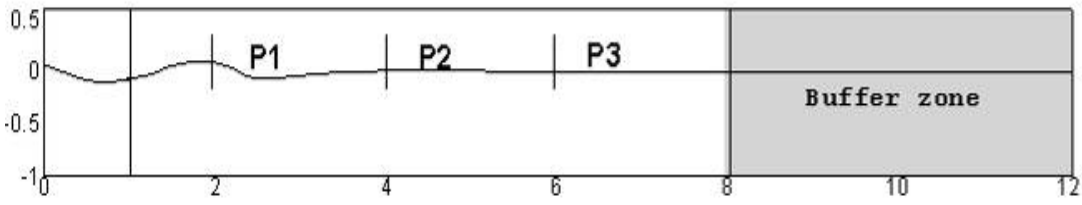

Figure 24 Schematic of wave flume and buffer zone implementation

The FANS program coupled with the level-set method computes the free surface, fluid velocities and pressures in three different coupled domains:

- Wave-maker domain—

The wave-maker domain is used to generate anticipated waves on the inflow boundary of the computational domain.

- Wave-tank domain—

The wave-tank domain is adjacent to the wave-maker domain. In this domain, the actual wave data of interest are computed and stored for further post-processing (wave elevation and velocity potential).

- Dissipation domain—

The dissipation damping domain is adjacent to the grid domain and is used to damp the wave components and to steady the water. This condition is accomplished by applying an explicit damping function.

Test 1 reduced the elements by one half in both the j and k directions, while Test 2 reduced the elements only in the j direction. Taking the same input wave as in the buffer zone study, the wave profiles at three gauges for these two tests are shown in Figure 25.

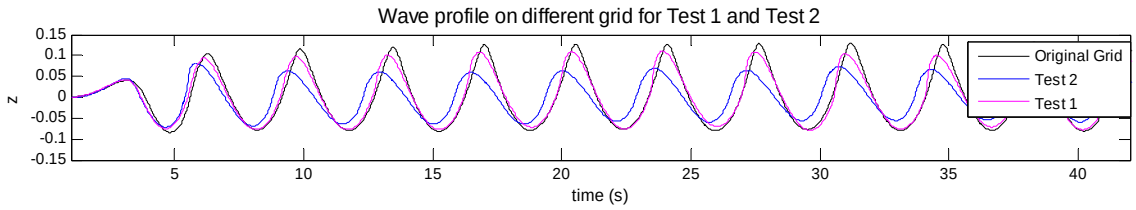

Figure 25 Wave profile on different grid for Test 1 and Test 2

By comparing the wave-height error for Test 1 and Test 2, we observe that the grid change in wave-height direction has more influence on the profile compared to the change in wave-length direction. According to this result, we designed three cases to achieve the most effective grid for our model.

To refine the grid, Table 3 shows the numerical simulation results for three grid sizes used in the wave tank. Errors and uncertainties due to grid size are estimated based on systematically refined grids with a constant refinement ratio:

Table 3 Grid density for Case 1, Case 2 and Case 3

Cases:	Type:	Cells in H	No. of Elements:
Cases 1(Original)	Coarse	20	290*84
Cases 2	Medium	30	290*126
Cases 3	Fine	40	290*169

After superimposing a sinusoidal wave at the wave maker for the three cases and applying an exponential damping function at the buffer zone, we computed wave elevations at three gauges for different mesh sizes (see Figure 26). The wave profile in the fine grid shows more properties of a nonlinear wave with the crests more sharply peaked and the troughs shallower and flatter. Figure 25 also shows that the wave profile observed in Case 2 and Case 3 do not have large differences. We could make the grid used in Case 3 sufficiently fine to accurately capture wave height in our model.

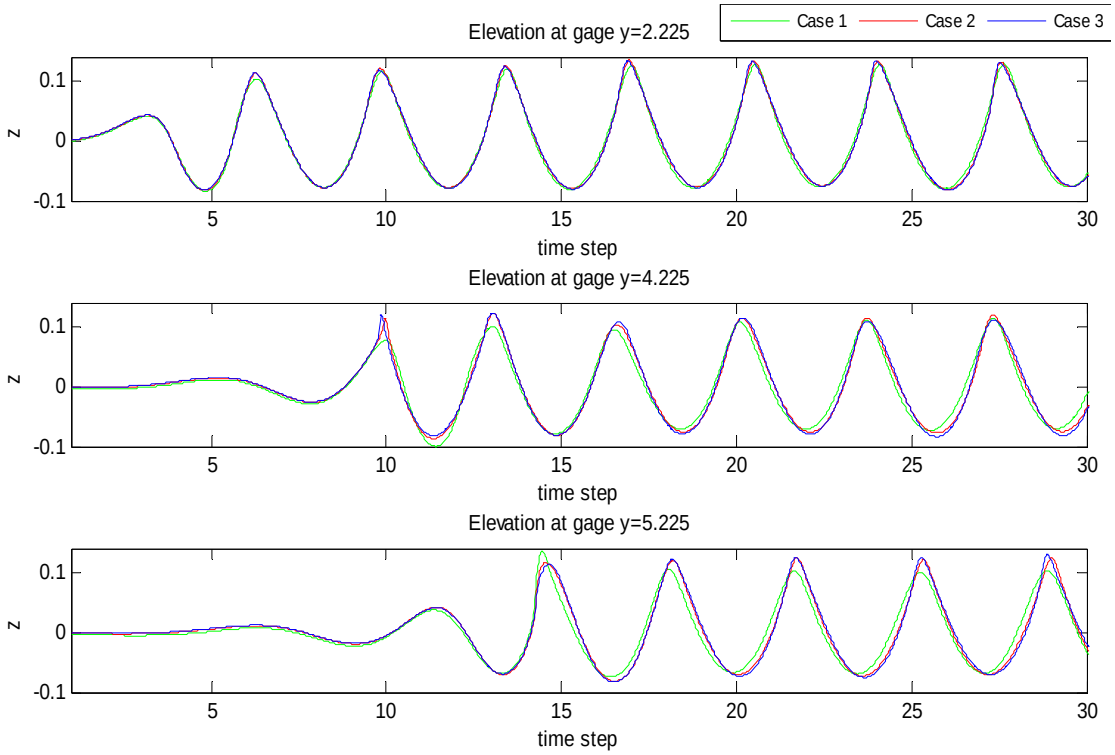

Figure 26 Comparison of wave elevations at three gages for different type of grid sizes

Wave shape evolves gradually when it transforms from a sinusoidal profile to a nonlinear profile. The wave shape can lose some nonlinear properties if the grid is not fine enough as shown in Figure 25.

Accuracy of the generated wave profile depends on grid density as well as the order of the simulation scheme. For small-amplitude waves, the smooth wave shape would be more accurately calculated by the higher order WENO scheme. As the grid becomes increasingly, sufficiently finer, the difference between the higher-order scheme and the lower one would decrease and finally approach zero. This condition would occur

because the difference in the higher-order scheme and lower one is proportional to the accuracy of scheme $O(\Delta x)^m$ (see Figure 27).

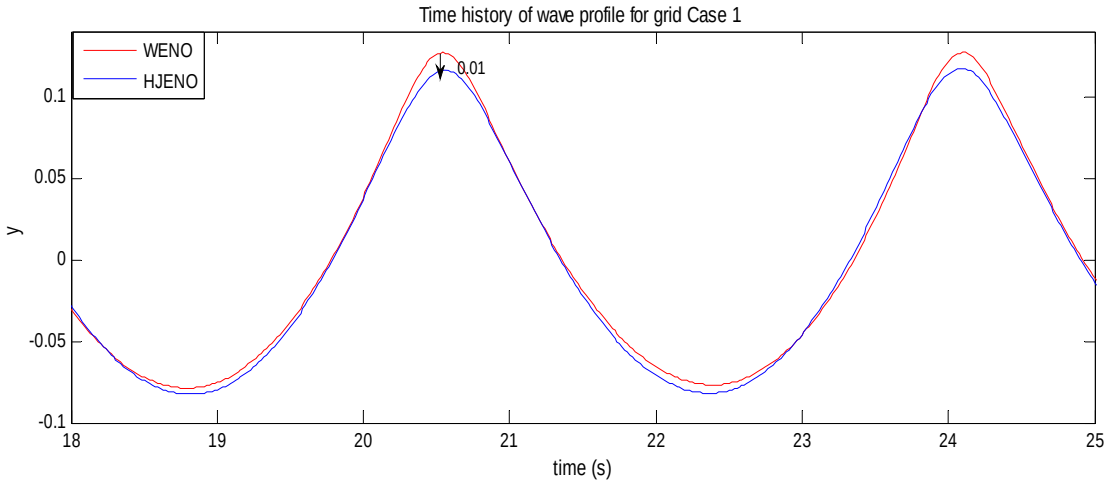

Figure 27 Time history of wave profile for WENO and ENO-3rd scheme on Grid Case 1

From this discussion, it has been shown that the periodic wave can be accurately simulated using the WENO scheme on a fine grid (290 x 169) when a proper exponential damping function is applied after the outflow of the computational domain.

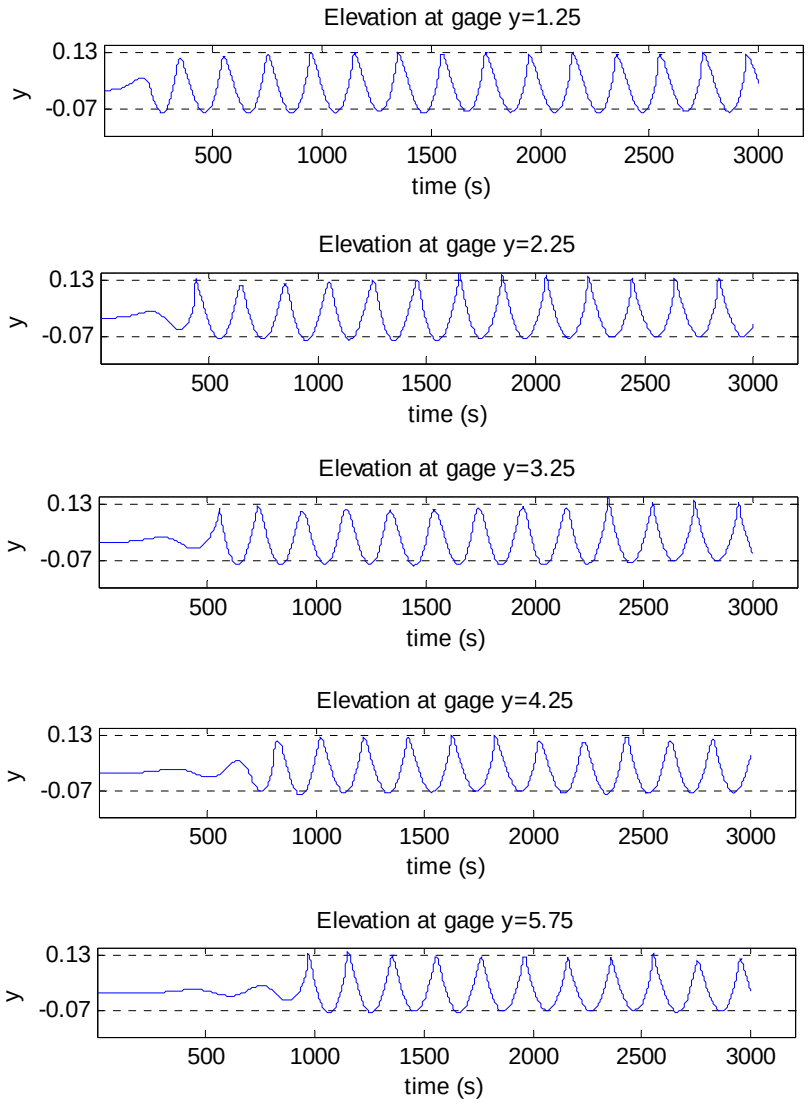

Figure 28 Time series of free surface elevation at different locations

CHAPTER V

BICHROMATIC WAVE INTERACTION AND EVOLUTION OF A BREAKING WAVE OVER A SLOPING BEACH

Numerical simulations of multi-component waves in a constant depth flume and breaking waves on a sloping beach are conducted to evaluate the performance of the present method. For a multi-peaked wave model, the instability of nonlinear wave interaction is investigated, and the features shown in our model are extremely compatible with theoretical solutions. Numerical tests also show that our model can accurately track breaking waves over sloping beaches. The breaking point is related to wave height and beach slope. We concentrate on two-dimensional results showing wave breaking and wave roll up.

Interaction of Bichromatic Waves in a Flat Flume

A spectral description of sea elevation is commonly used to predict loads on offshore structures due to surface waves. This approach is based on the superposition of the linear wave model. Recently, the ‘‘freak’’ waves (or rogue waves) phenomena has resulted in more attention being placed on this widely used approach and researchers have started to investigate the formation of these “freak” waves. Chaplin (1996) showed that focused component waves are fully nonlinear in a relatively small region. From his experimental results, there is a high-frequency range produced, well above the input spectrum. A non-negligible amount of energy exists at these new frequency components. Onorato et al. (2006) recently developed a simple weakly nonlinear model for two

nonlinearly interacting water waves in deep water with two different directions of propagation. They showed that the dynamics of these coupled waves are governed by two coupled nonlinear *Schrödinger* (CNLS) equations. Other research groups also identified the nonlinearity of wave interaction. These research groups showed that large-amplitude freak waves in the oceans can be produced by the nonlinear instability of water interacting nonlinearly in a constructive way.

We tried to investigate the properties of nonlinearly interacting water by coupling the directional wave simulation (DWS) (Huang and Zhang, 2009) with our RANS solver. The DWS program numerically simulates the time series of the irregular waves in different locations based upon the directional wave energy spectrum.

To have a better comparison of wave patterns between DWS domain with liner wave and RANS domain with nonlinear wave, we increased the wave-maker domain size for the test model described in Chapter IV as DWS domain, and set the RANS domain to the same size begins immediately after it. The wave-maker domain, which is applied with the DWS program, is 400 m long and 1,600 m high. We used the water depth as the normalization factor. Numerical simulation is based on the same grid density as Case 3 in Chapter IV, which is uniform in the x-direction at $\Delta x = 0.0125$ and stretched in the y-direction from the finest size, $\Delta y = 0.005$ in the mean-water area, to $\Delta y = 0.1$ at the top and bottom. In the wave-maker domain, we reduced the grid density in most of the area to one-half of the original value and keep the overlap area with the wave tank unchanged (see Figure 28).

Because the DWS program provides an exact solution for every point in the domain, it is not an effective way to apply a fine grid to obtain the contour of the wave profile. By covering only the overlap region with a fine grid, we could still obtain an accurate solution with less computer costs. Also, four gauges were set up in the wave-maker domain and the computational domain to measure water elevation history (see Figure 29 and Figure 30).

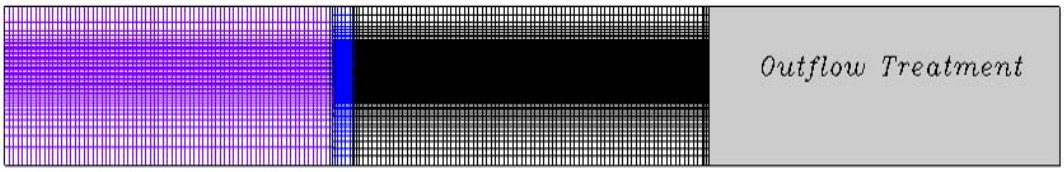

Figure 29 Numerical grid for bichromatic wave interaction case

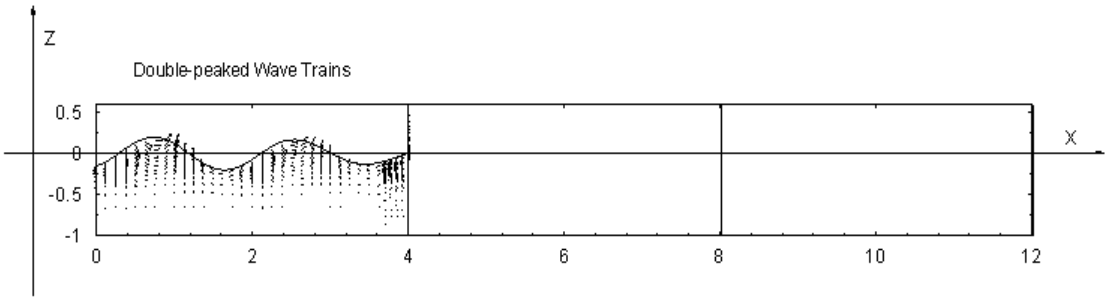

Figure 30 Flume Configuration

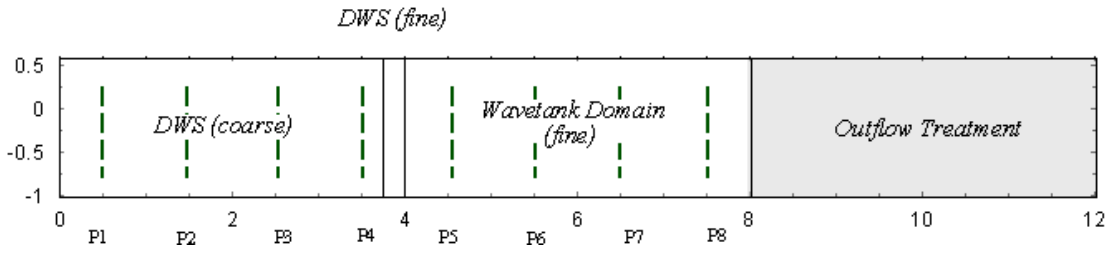

Figure 31 Schematic of Program DWS and buffer zone implementation

To compare the single-wave and group-wave cases composed by these single waves, we also ran simulations where Wave 1 and Wave 2 were generated separately in the same model. For the purpose of this study, the input for biochromatic waves was made up of frequencies σ_1=0.0882 s^{-1} and σ_2=0.098698 s^{-1} and spectrums S_1=90.0 m^2 and S_2=72.000 m^2. The group wave value was calculated by superposition at a water depth of 100.0 m. Figure 31 shows the wave profiles of these two waves and the group profile obtained by superposition. We compared the profile changes for single waves and their combined group wave. The group wave calculated by nonlinear code maintained a similar group property as the one obtained from the DWS program. Another factor requiring additional attention is that the profiles provided in Figure 32 for the computational domain are measured at a gauge located relatively close to the wave maker, which might not have performed nonlinearly.

To obtain a more complete understanding about the instability and evolution of nonlinearly interacting water waves, we compare the time history of wave elevation at gauges $P1_1$(x = 2.25L), $P1_2$(x = 2.75L), $P1_3$(x = 3.25L), and $P1_4$(x = 3.75L) (wave length L=2.0).

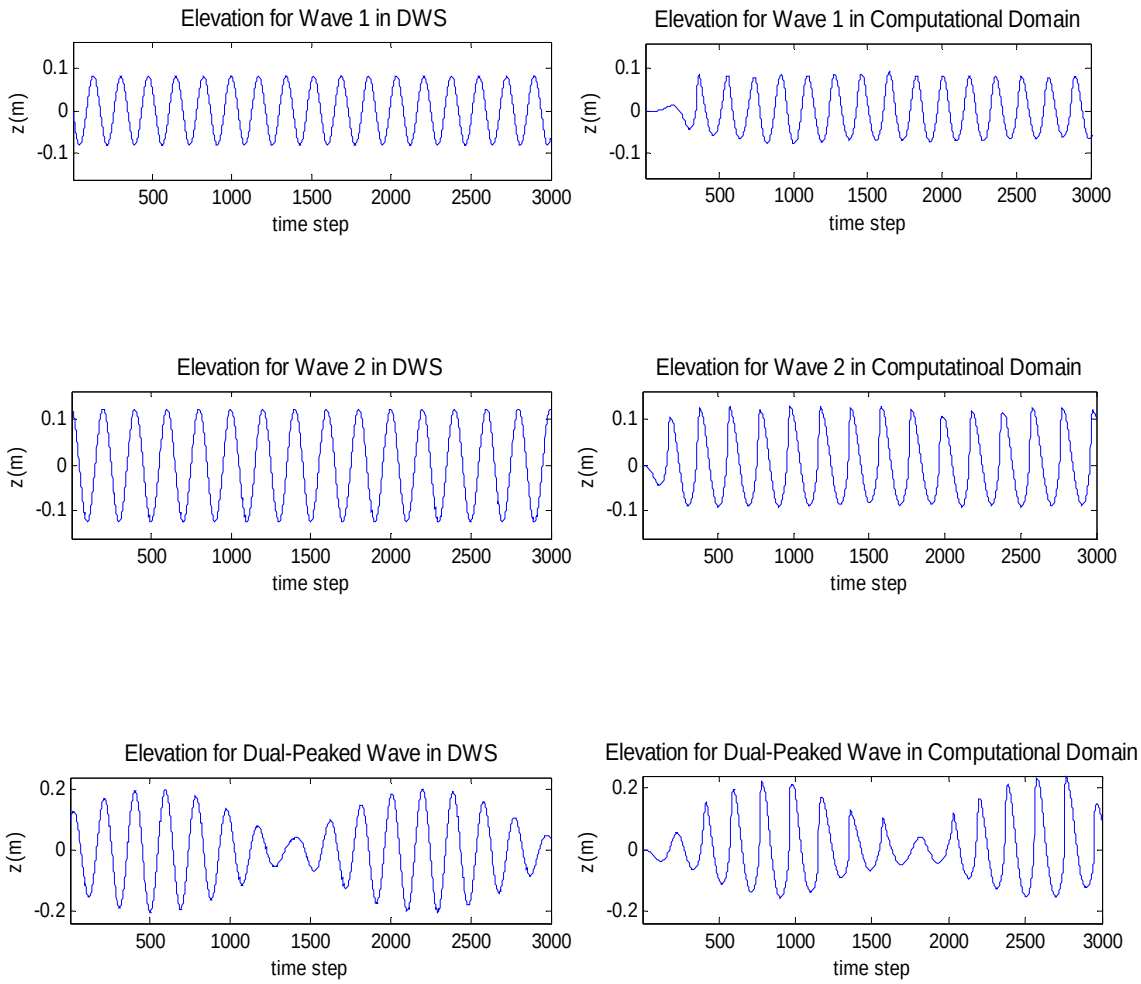

Figure 32 Comparison for single wave and group wave computed by DWS and RANS

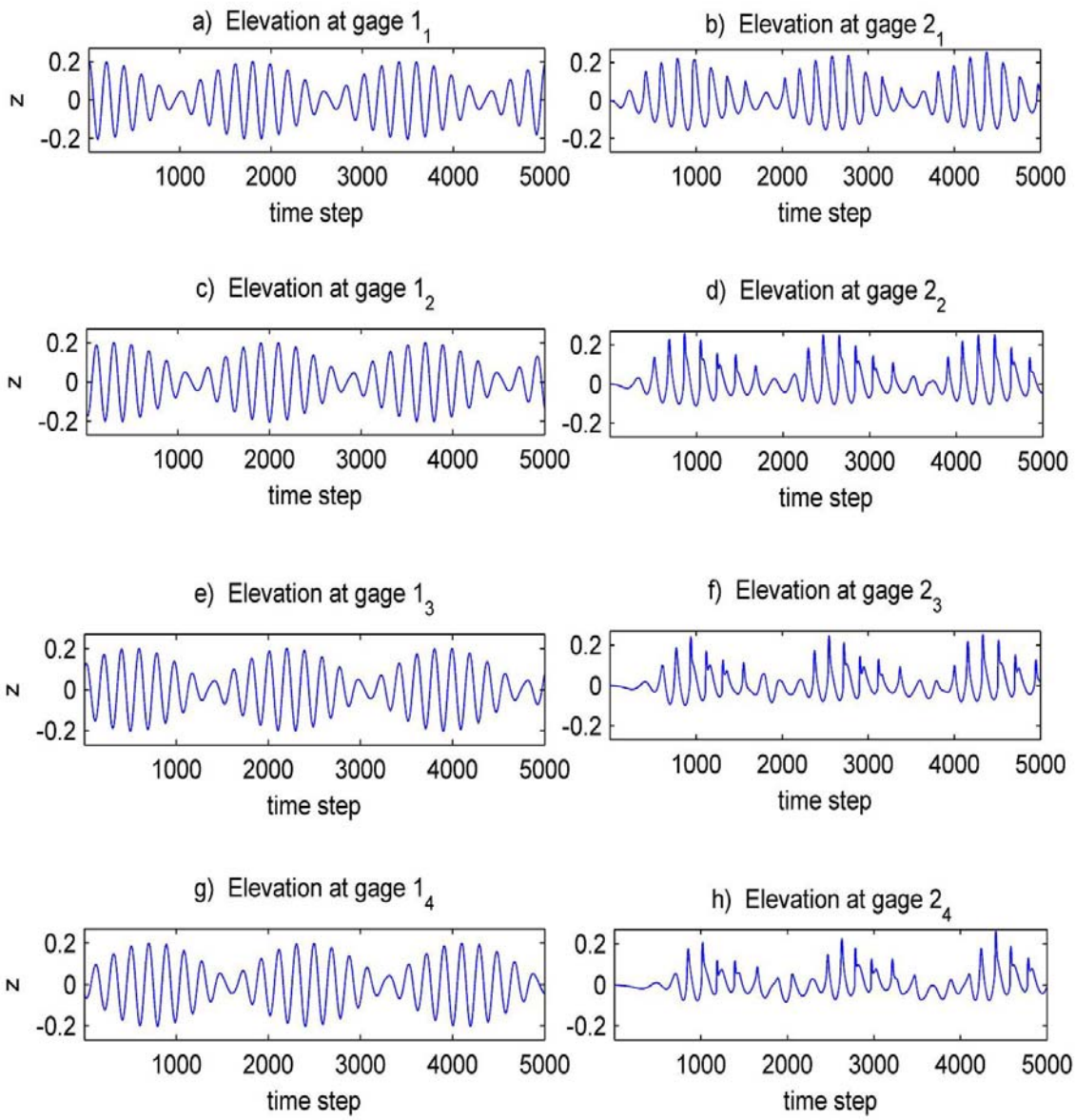

Figure 33 Sinusoidal input (left-hand column) and simulated input using RANS (right-hand column) surface elevation

A general view of the free-surface time and spatial evolutions at the four gauges is shown in Figure 33 and Figure 34. Each figure shows that the overall free surface is in a strong wave-grouping pattern. Evolution of nonlinear interaction waves along the wave flume shows more instability, compared with the linear group wave profile obtained by superposition. This is due to the coupling and interaction of the two nonlinear waves. The maximum wave height (Figure 33) is $H2_{max} = 2.6$, while the superposed maximum wave height is $H1_{max} = 2.0$ in the wave maker. Comparing the wave shapes at the four gauges, the amplitude spectrum is modified dramatically only in approximately one wave length. Figure 33-f and Figure 33-h show the same pattern, which means that the free surface of the wave group has been relatively stable before the second wave length. The free surface envelope becomes more asymmetrical. Figure 33-f shows that the crest gradually moves to the left in each group as the wave propagates. The temporal variation of the surface elevation for Gauge 4 under fully nonlinear performance is presented in Figure 33-h. Similar left-right asymmetry, which is manifested in our simulation, was also identified by the theoretical simulations based on the Zakharov model (Shimer, 2000). Another phenomenon during this wave interaction is that the group wave envelope has phase shift compared to the superposition of two single nonlinear waves shown in Figure 33 and Figure 35.

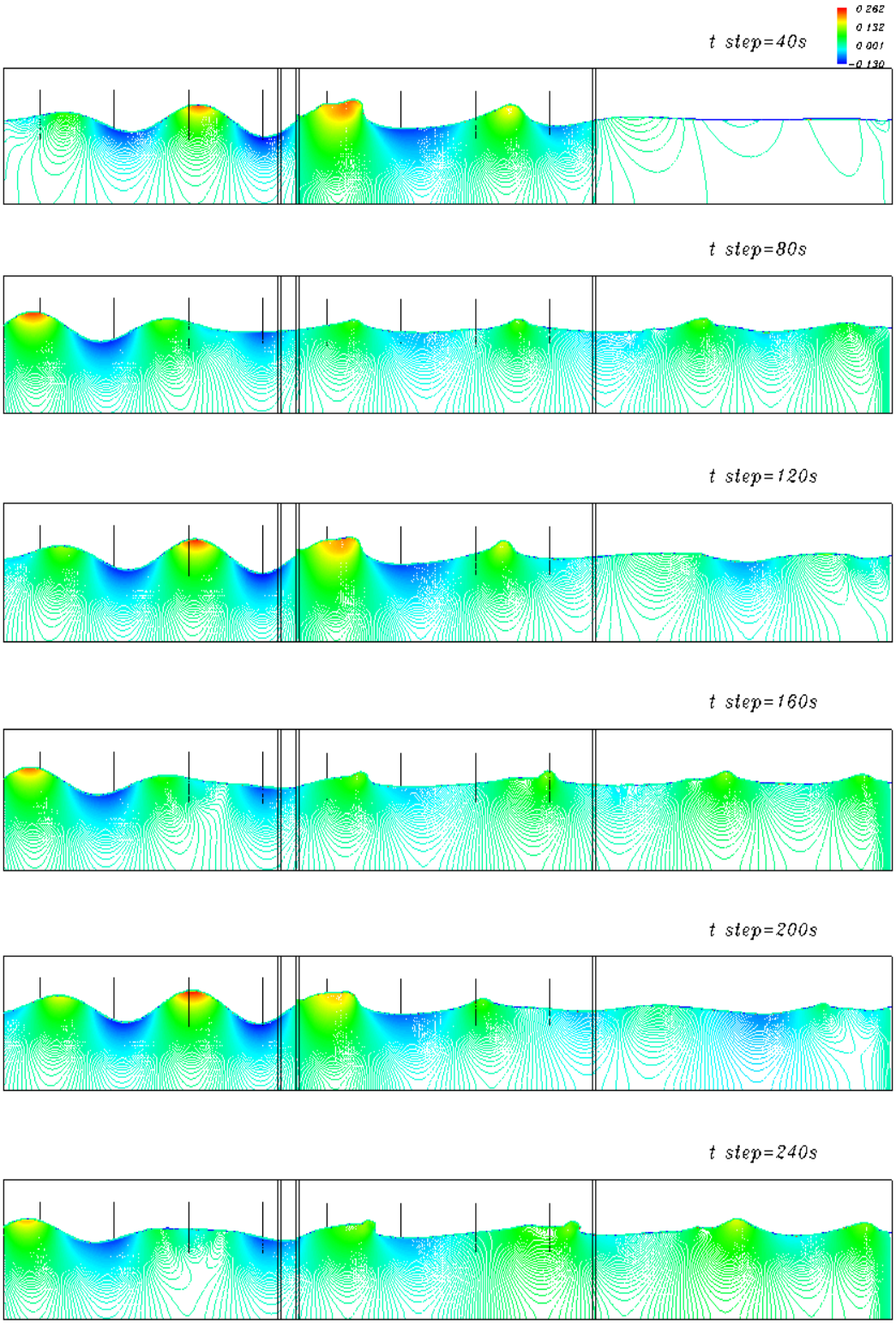

Figure 34 The interaction between two nonlinear waves

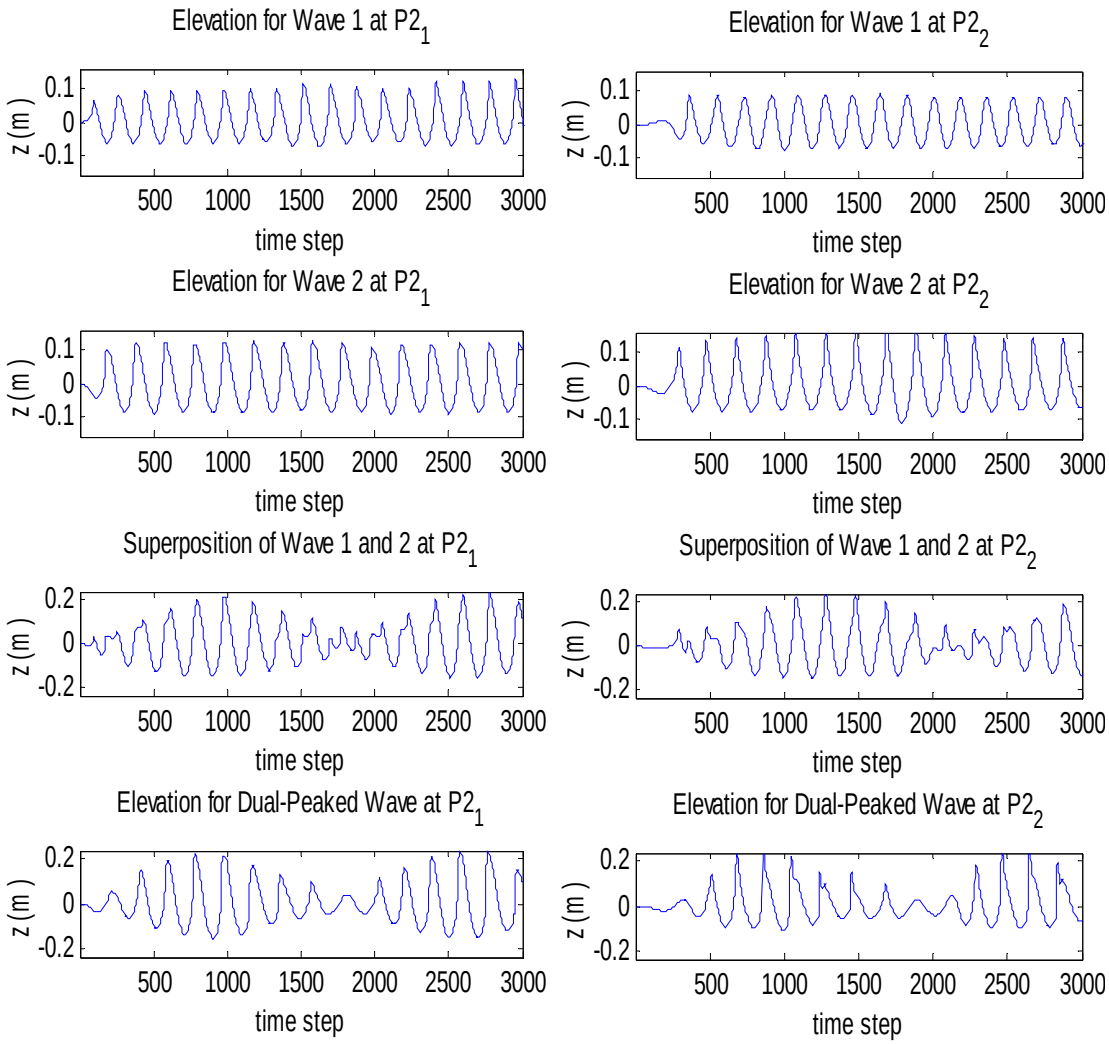

Figure 35 Comparison of single nonlinear waves superposition and simulation free surface

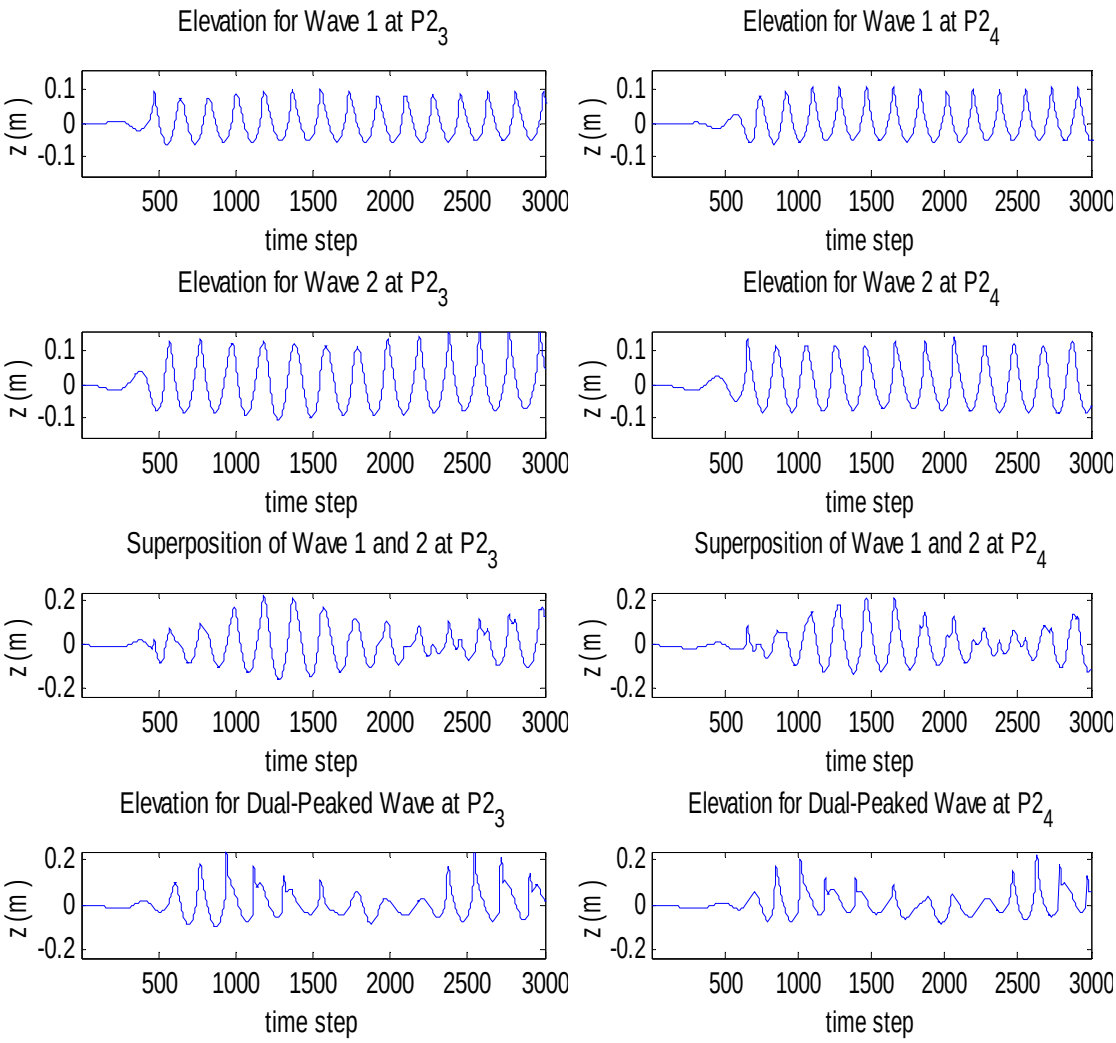

c) d)

Figure 35 (continued)

In summary, we have presented a numerical study of the instabilities of two nonlinearly interacting, two-dimensional waves in deep water. Laboratory simulation of dual-wave-train shoaling and breaking on a plane beach indicates that simple approaches to estimating the transformation, such as linear superposition of single wave trains, will not work. Numerical analysis of the full dynamical system reveals that two water waves can produce large waves compared to initial waves when nonlinear interactions are taken into account.

Evolution of Breaking Waves over a Sloping Beach

In this test, a sinusoidal wave was generated and propagated in the computational domain with a sloping bottom by solving the numerical model using the fifth-order WENO Runge-Kutta scheme. The calculation domain begins at x = 0.0 m from the toe of the slope, which is 15 m long and starts from a height of 1.5 m.

A refined grid (Figure 36) has been made according to the maximum wave height prior to the seawall and according to maximum velocity modulus beyond that point. The calculation domain is built with 300 cells in the x-direction and 60 cells in the z-direction, except for the region near the seawall, which was re-gridded to 100 cells in the z-direction. The grid sizes were set to $\Delta x = 0.05$ m, $\Delta z = 0.15$ m at coarsest part, and $\Delta z = 0.015$ m at the coarsest part.

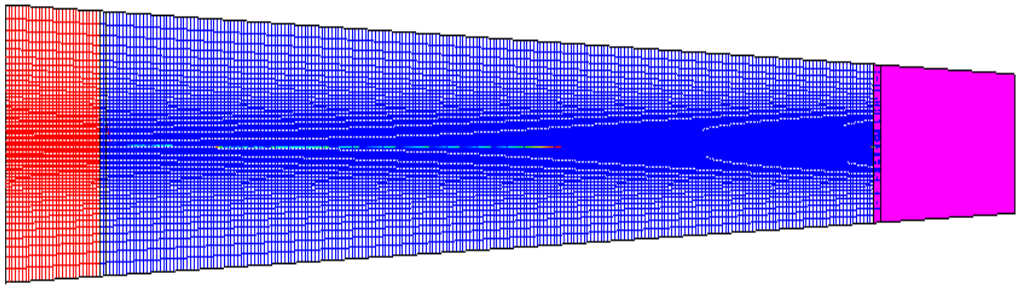

Figure 36 Typical mesh for 2D surf zone (Refine mesh near the free surface)

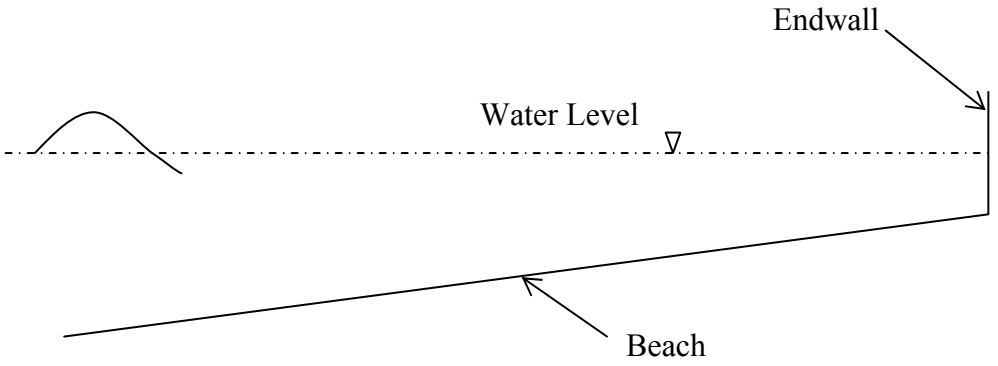

a) 2D schematic diagram for surf zone

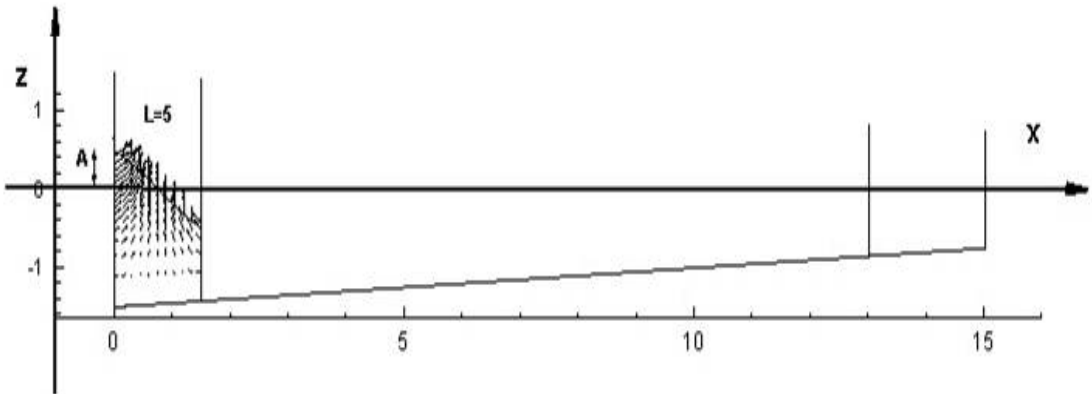

b) Dimension for surf zone

Figure 37 Sketch for model set up on sloping beach

Numerical simulations were conducted separately on three different sloping beaches with 1/20 and 1/15 slopes under the same input wave trains (Table 4). The bottom topography plays an important role on the change in wave-breaking characteristics (Garzon and Sethian 2006). To study the dependency of wave breaking as a function of these different beaches, we tested the following cases:

Table 4 Slope and input wave height for all the cases

	slope =1:20	slope =1:15
Ho = 0.57	Case 1	Case 2
Ho = 0.65	Case 3	Case 4
Ho = 0.70	Case 5	Case 6

Figure 37 shows an example of the simulated results for Case 4. Waves break on a 1/15 slope at breaking point x_b = 6.6 m with the breaking wave height H_b = 0.413 m. Using a different color, Figure 38 shows simulated instantaneous surface elevations from the shoaling region to the bore region on sloping beaches. The surface elevations are typical shallow-water waves with higher wave crests and flatter wave troughs. As the waves shoal, the wave crests become even more peaked with increasing wave height until a maximum height occurred at x= 6.6 m where a vertical front is reached, tangent to the calm water surface. This is usually called the breaking point, BP= (t_{bp}, x_{bp}, z_{bp}), where x_{bp} represents the x coordinate, z_{bp} the height at x_{bp}, and t_{bp} the time of

occurrence. Beyond the BP, a wave tip develops and velocities are much greater than the wave celerity, which causes wave overturning and subsequent falling of the jet toward the flat water surface. This end point is denoted as EP= (t_{ep} , x_{ep}).

From the simulated result shown in Figure 39-44 and Table 5, wave shape and breaking characteristics are related to wave height and beach slope. On steeper beaches, waves break earlier with higher breaking point heights. Also, the breaking wave occurs slightly closer to the wave maker, but it needs a longer time to reach the end point for the same breaking wave.

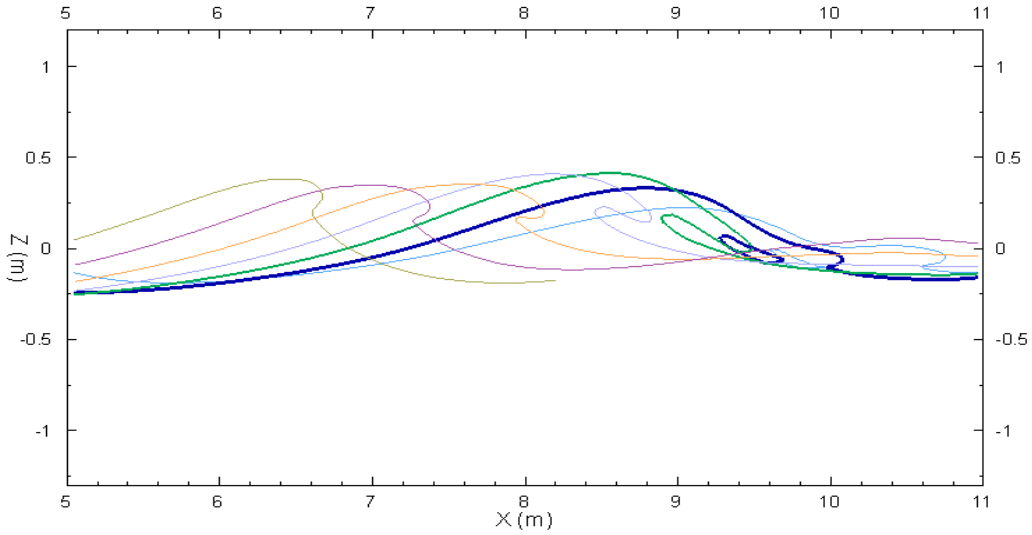

Figure 38 Wave shape at consequent times (Case 2)

Table 5 Breaking characteristics

		t_{bp} (s)	x_{bp} (m)	z_{bp} (m)	t_{ep} (s)	x_{ep} (m)
Second Wave Peak	1	8.8934	3.91	0.50	12.3318	7.89
	2	9.1772	4.00	0.49	12.5000	8.15
	3	8.6000	3.51	0.54	10.6110	6.20
	4	8.6040	3.52	0.54	10.6200	6.25
	5	8.3168	3.32	0.60	10.0375	5.61
	6	8.8904	3.79	0.51	10.6111	6.20
Third Wave Peak	1	15.4865	4.65	0.49	19.5015	9.22
	2	16.3468	5.52	0.48	20.0751	9.78
	3	14.9500	4.20	0.52	17.2072	7.27
	4	14.9129	4.23	0.50	17.4000	7.50
	5	14.0400	3.25	0.63	15.7800	5.65
	6	14.0525	3.43	0.60	16.0601	6.08

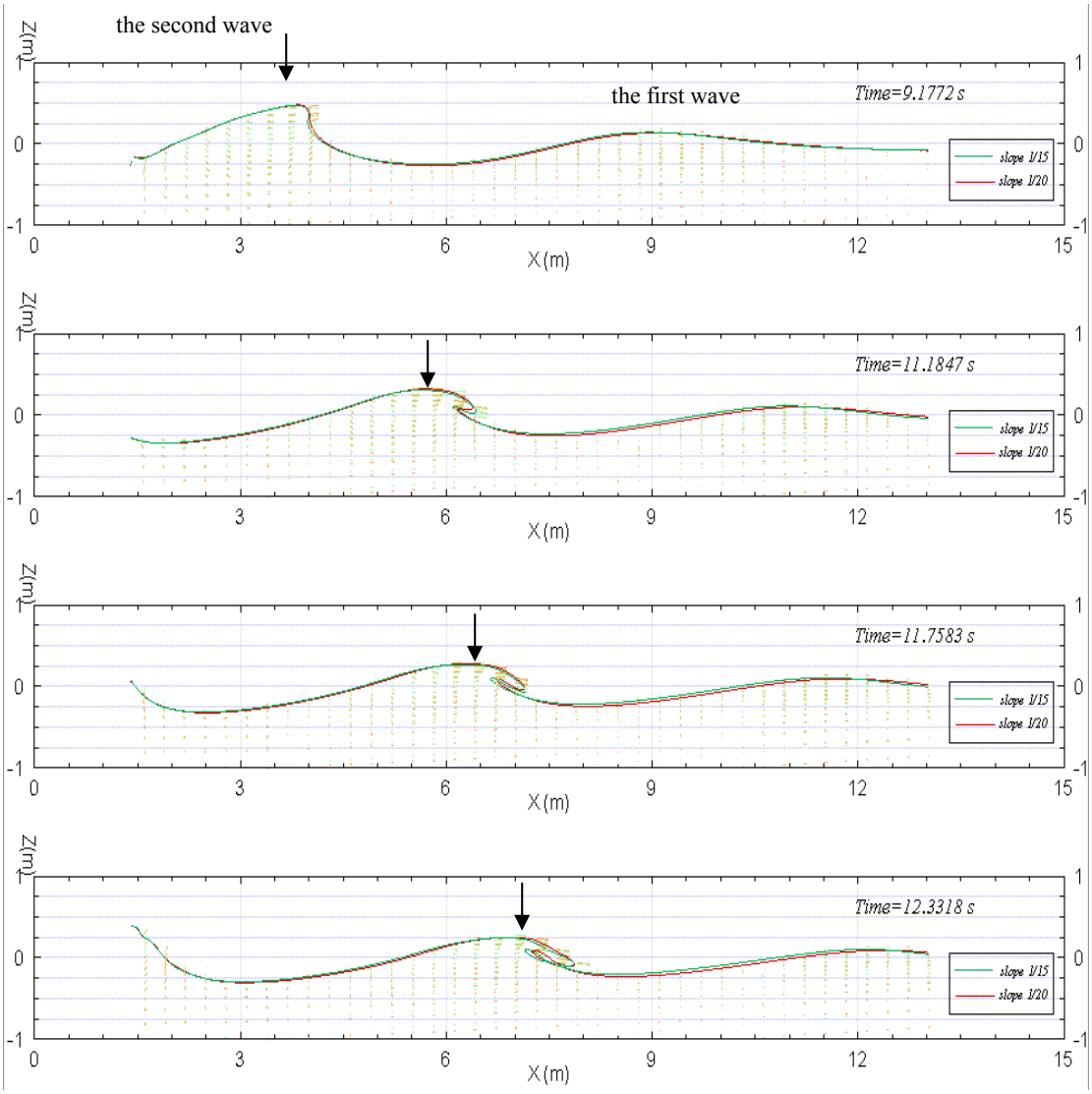

Figure 39 Propagation of the second wave crest on beaches with slopes 1/15 and 1/20 (Ho=0.57)

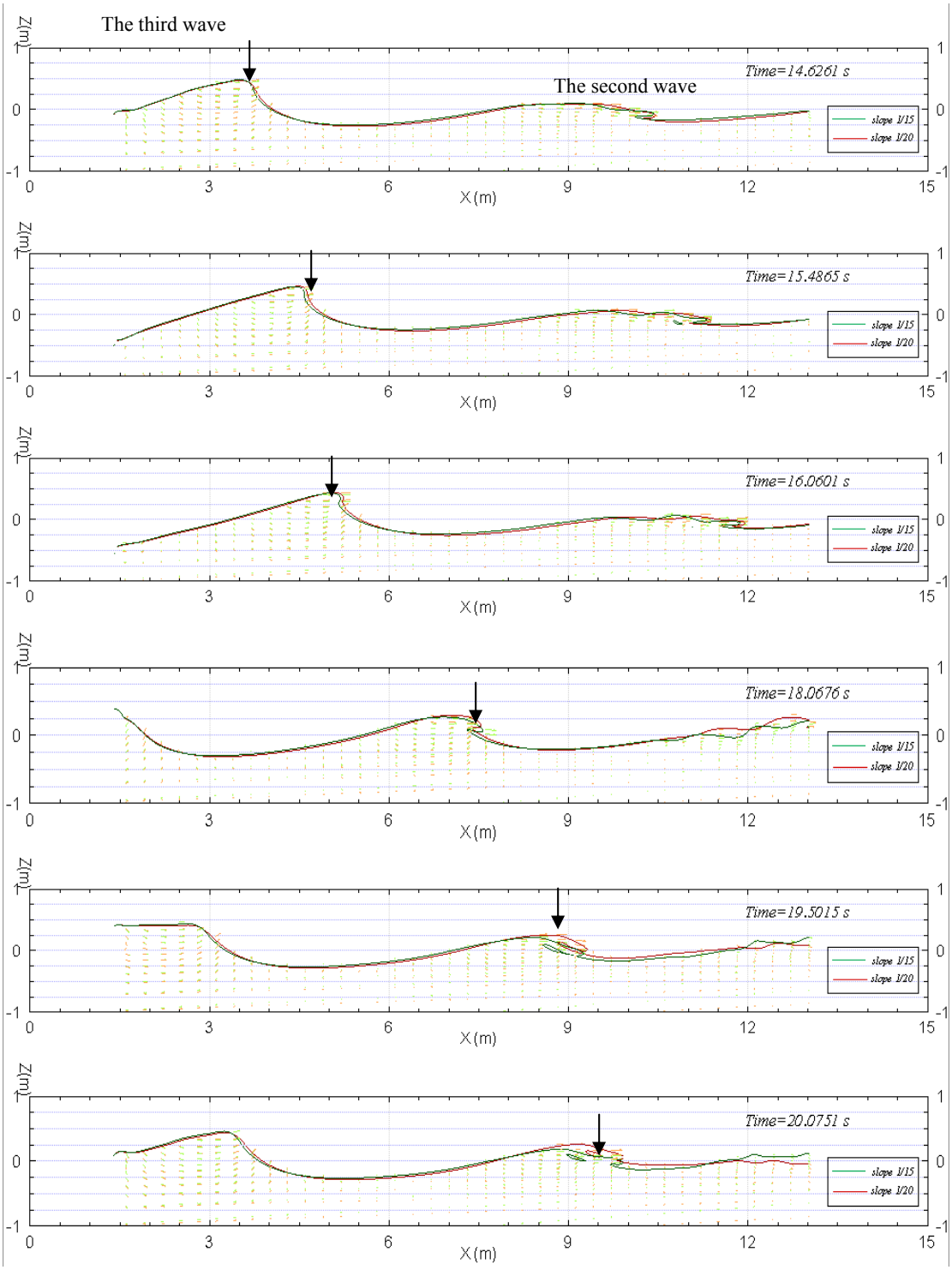

Figure 40 Propagation of the third wave crest on beaches with slopes 1/15 and 1/20 (Ho=0.57)

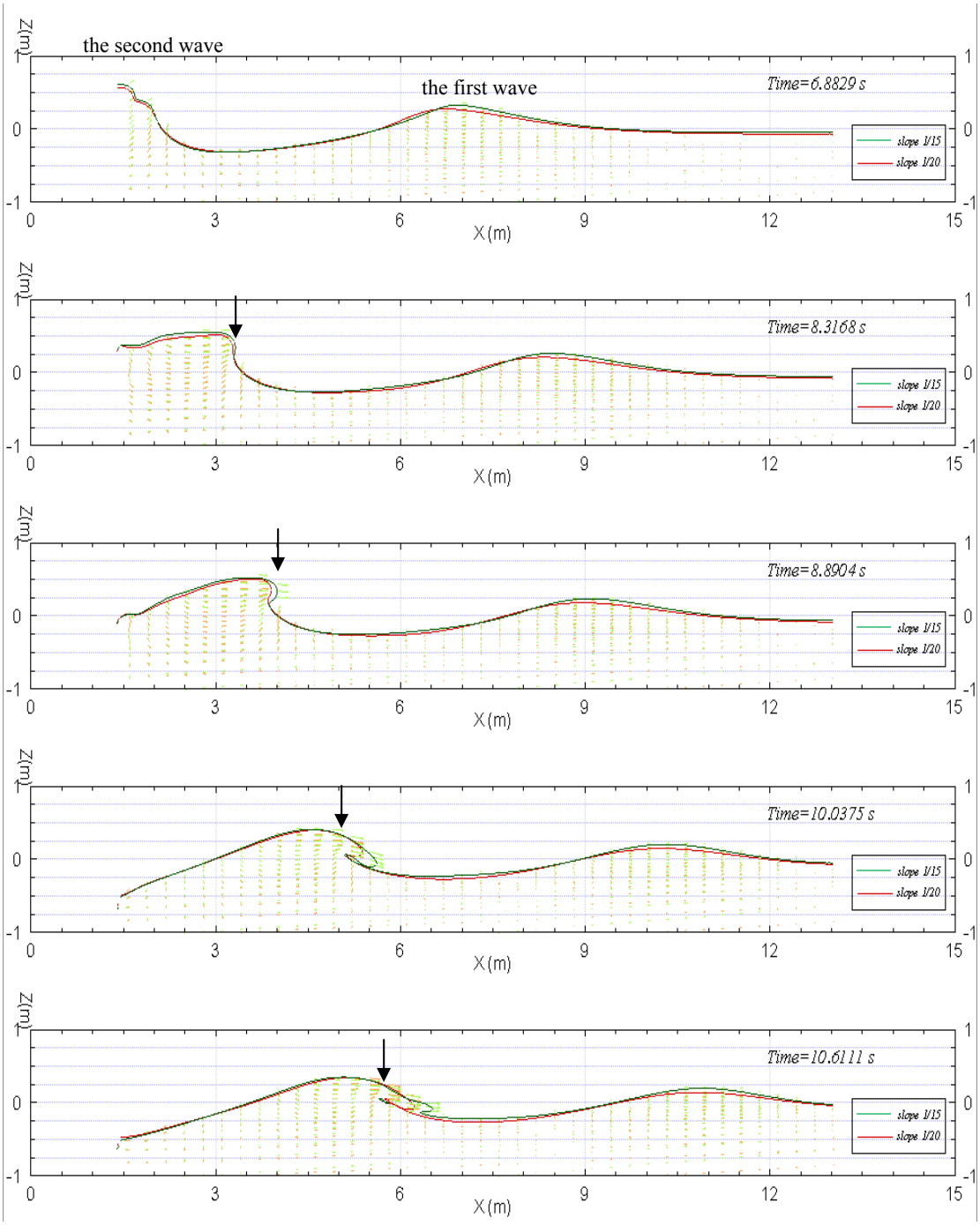

Figure 41 Propagation of the second wave crest on beaches with slopes 1/15 and 1/20 (Ho=0.65)

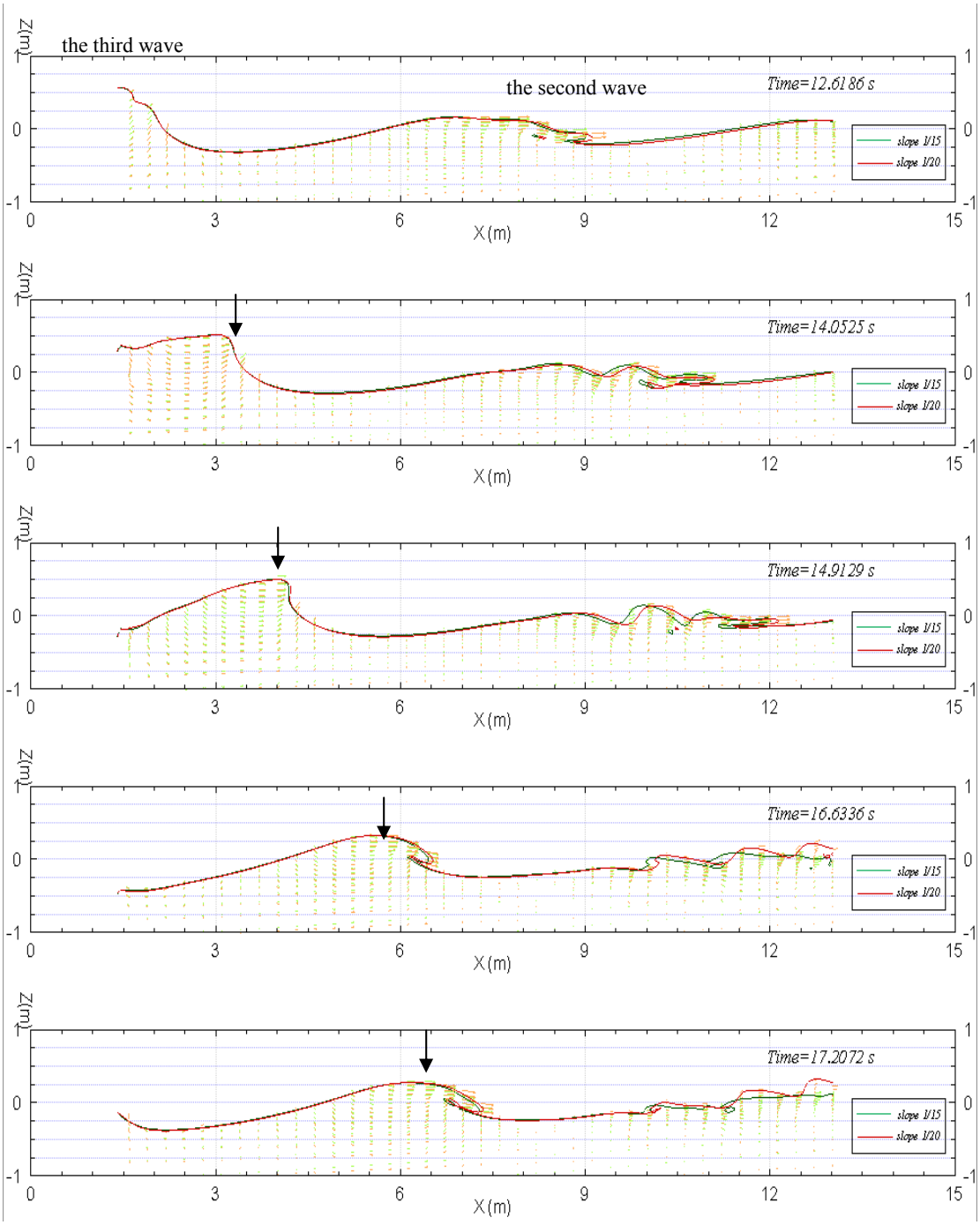

Figure 42 Propagation of the third wave crest on beaches with slopes 1/15 and 1/20 (Ho=0.65)

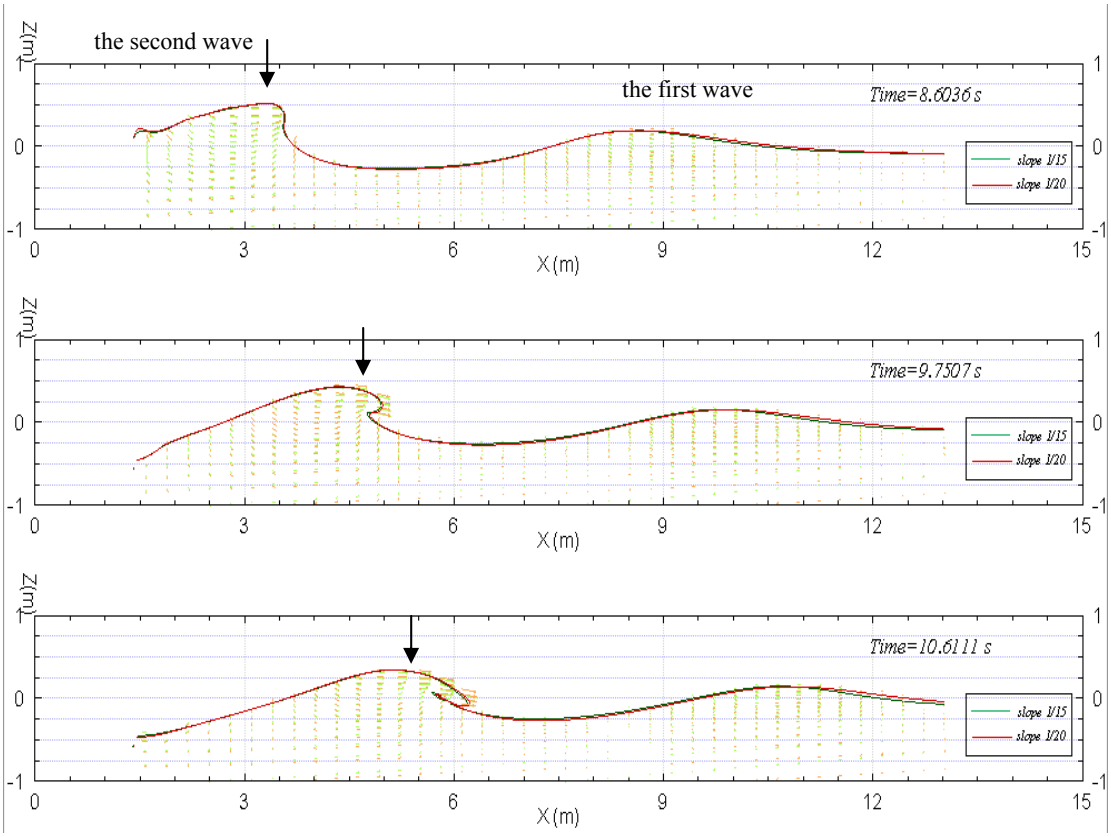

Figure 43 Propagation of the second wave crest on beaches with slopes 1/15 and 1/20 (Ho=0.70)

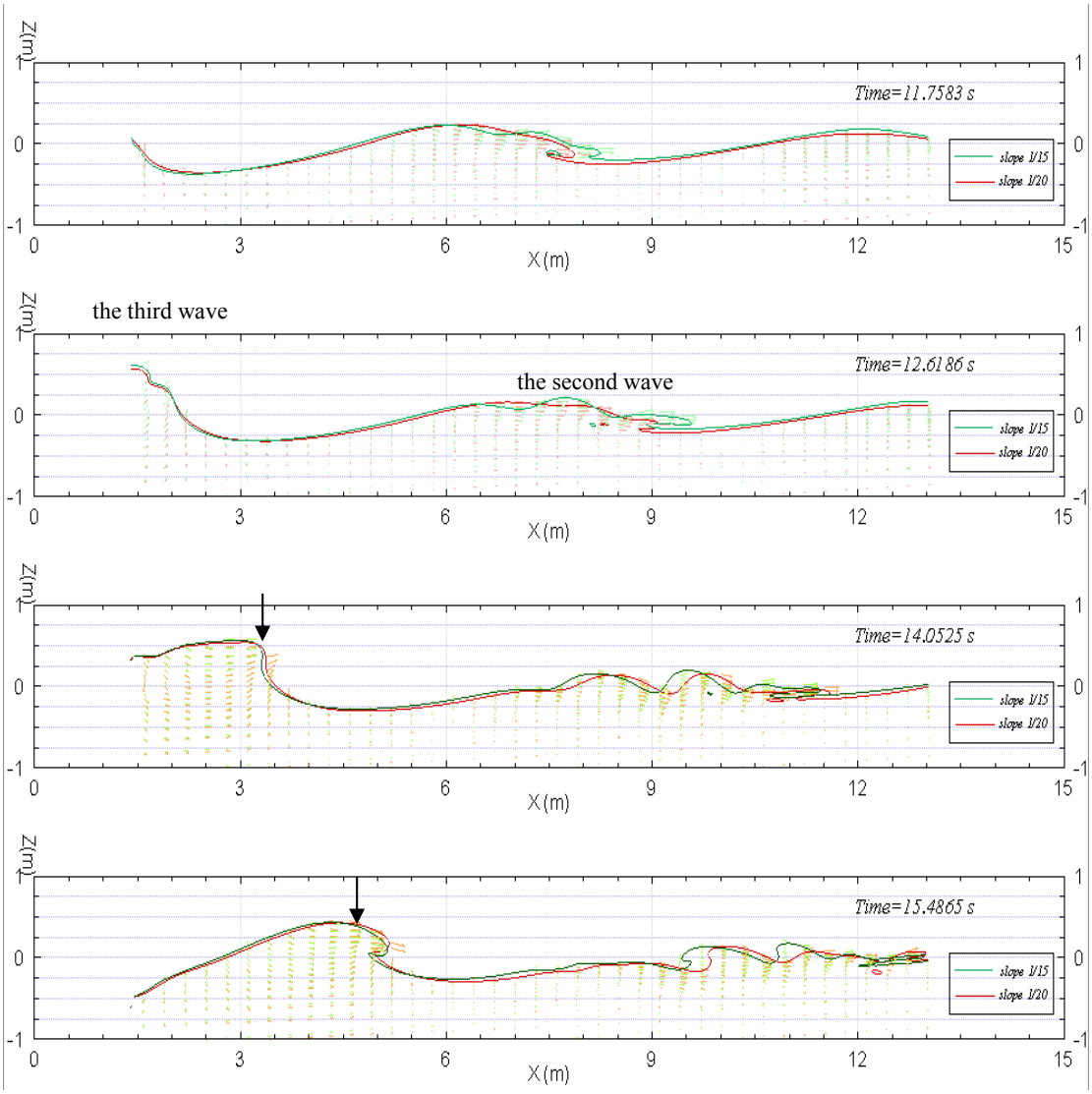

Figure 44 Propagation of the third wave crest on beaches with slopes 1/15 and 1/20 (Ho=0.70)

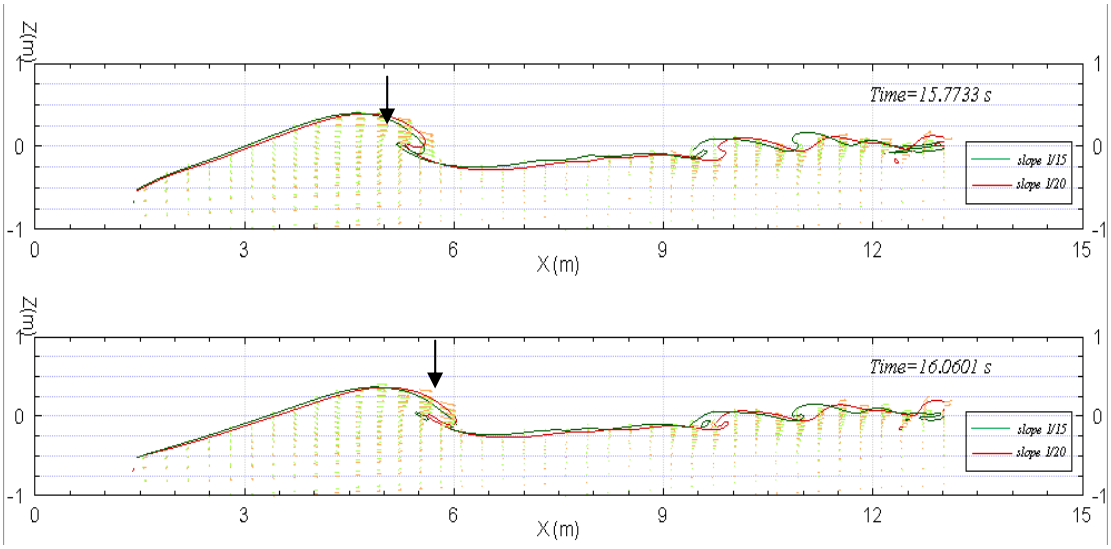

Figure 44 (continued)

Wave shape and breaking characteristics are related to wave height and beach slope. On steeper beaches, waves break earlier with higher breaking point heights. Also, the breaking wave occurs slightly closer to the wave maker, but it needs a longer time to reach the end point for the same breaking wave.

CHAPTER VI

CONCLUSIONS

In the present study, a numerical wave tank containing a viscous fluid was used to simulate the propagation of water waves over a sloping beach. In this numerical scheme, the unsteady RANS equations were solved for the mean flow field and its dissipation. A level-set method was adopted for capturing the interface between the air and water phase.

A numerical wave tank was used to investigate the propagation of bichromatic waves and breaking waves over a sloping beach. To present the capability of the numerical model, a series of experiments were performed and conclusions of this study follow:

1. Zalesak's problem was performed to examine the level-set method. By comparing the numerical results of the level-set method by adopting the WENO scheme with traditional level-set method with the ENO scheme it was revealed that the higher order level-set method substantially eliminated the diffusion in sharp corners of the traditional level-set method.

2. The accuracy of the numerical results obtained by applying the WENO scheme for the incident wave profiles were verified by comparing numerical results with solutions obtained using the ENO scheme. The characteristics of nonlinear monochromatic waves were studied systematically and comparisons were conducted. To eliminate other factors that can produce fluctuations on the wave profile, different damping functions and grid densities were studied. The comparisons revealed that the

present numerical results are sufficiently efficient to improve the accuracy of the level-set RANS method.

3. For a surface-tracking numerical method built on curvilinear coordinates, the level-set RANS model was tested for nonlinear bichromatic wave trains and breaking waves on sloping beaches with complex free surfaces. The velocity of the fluid flow surface became complicated as the wave breaks. The level-set finite-analytic Navier-Stokes (FANS) numerical model performed well in simulating the two-phase flow velocity and its corresponding surface evolution when the water wave passed over the different sloping beaches. Wave-breaking characteristics in the test cases provided an efficient technique to capture the surface accurately. Different wave heights and beach slopes were used for predicting and simulating the breaking points. The results show that the dependency of wave shape and breaking characteristics to wave height and beach slope match the results provided by Garzon and Sethian. (2006).

4. A Navier-Stokes numerical model combined with level-set method was applied to investigate waves over a sloping beach. Using the present numerical model, the complete evolution of an overturning wave were captured, including the initial stage of incident wave, shoaling process, wave breaking, re-attachment, air entrainment, and splash-up phenomena. The relationship between the initial wave height, beach slope, and breaking wave characteristics were discussed. The numerical results showed that on steeper beaches, waves break earlier with higher breaking point heights. Also, the breaking wave occurs slightly closer to the wave maker, but it needs a longer time to reach the end point for the same breaking wave.

REFERENCES

Amsden, A. A., and Harlow, F. H. (1970). "SMAC method: A numerical technique for calculating incompressible fluid flows." *Los Almos Scientific Laboratory*, University of California.

Brackbill, J.U., Kothe, D.B., and Zemach, C. (1992). "A continuum method for modeling surface tension." *J. Comput. Phys*., 100, 335-353.

Bradford, S.F. (2000). "Numerical simulation of surf zone dynamics." *J. Waterway, Port, Coastal and Ocean Eng.*, 126(1), 1 –13.

Chang, Y.C., Hou, T.Y., Merriman, B., and Osher, S. (1995). "A level set formulation of Eulerian interface capturing methods for incompressible fluid flows." *J. Comput. Phys*., 124, 449-464.

Chaplin, J.R. (1996). "On frequency-focusing unidirectional waves." *Inter. J. Offshore and Polar Eng.,* 6(2), 131–137.

Chen, H.C. and Chen, M. (1998). "Chimera RANS simulation of a Berthing DDG-51 ship in translational and rotational motions." *Inter. J. Offshore and Polar Eng.*, 8(3), 182-191.

Chen, H.C., Liu, T., Huang, E.T., and Davis, D.A. (2000). "Chimera RANS simulation of ship and fender coupling for berth operations." *Inter. J. Offshore and Polar Eng.*, 10(2), 112-122.

Chen, H.C., and Patel, V.C. (1989). "The flow around wing-body junctions." *Proc., 4th Symposium on Numerical and Physical Aspects of Aerodynamic Flows*, Long Beach, CA, 16-19.

Chen, H.C., Patel, V.C., and Ju, S. (1990). “Solutions of Reynolds-averaged Navier-stokes equations for three-dimensional incompressible flows." *J. Comput. Phys.*, 88, 305-335.

Chen, H.C., Yu, K. (2006). “Numerical simulation of wave runup and greenwater on offshore structures by a level-set RANS method.” *Proc., 16th Int. Offshore and Polar Eng. Conf., vol. III*, San Francisco, CA, 185–192.

Chen, S., Johnson, D.B,, and Raad, P.E. (1991). “The surface marker method.” *Comput. Modeling of Free and Moving Boundary Prob.*, 1, 226–234.

Christensen, E.D., and Deigaard, R. (2001). “Large eddy simulation of breaking waves.” *Coastal Eng.*, 42, 53–86.

Christensen, E.D., Jensen, J.H., and Mayer, S. (2000). “Sediment transport under breaking waves.” *Proc., 27th Int. Conf. on Coastal Eng.*, ASCE, Sydney, Australia, 2467– 2480.

Enright, D., Fedkiw, R., Ferziger, J., and Mitchell I. (2002). “A hybrid particle level set method for improved interface capturing.” *J. Comput. Phys.*, 183, 83-116.

Ewing, L. (2009). “Field investigation of Hurricane Ike impacts to the upper Texas coast.” *Shore & Beach*, 77(2), 9-23.

Ferziger, J.H., and Peric, M. (1999). *Computational methods for fluid dynamics*, Springer-Verlag, Berlin.

Garzon, M., and Sethian, J.A. (2006). “Wave breaking over sloping beaches using a coupled boundary integral-level-set method.” *Int. Series of Numer. Math.*, 154, 189-198.

Harlow, F., and Welch, J. (1965). “Numerical calculation of time-dependent viscous incompressible flow of fluid with a free surface.” *The Phys. Fluids*, 8, 2182–2189.

Hirt, C. W., and Nichols, B. D. (1981). "Volume of fluid (VOF) method for the dynamics of free boundaries." *J. Comput. Phys.*, 39, 201–225.

Huang, L., and Zhang, J. (2009). "Introduction to program DWS (Directional Wave Simulation)." Technical Report, Ocean Engineering Program, Texas A&M University, College Station, Texas.

Jiang, G., and Peng, D. (2000). "Weighted ENO schemes for Hamilton–Jacobi equations." *SIAM J. Sci. Comput.*, 21, 2126–2143.

Jiang, G., and Shu, C.W. (1996). "Efficient implementation of weighted ENO schemes." *J. Comput. Phys.*, 126, 202–228.

Lemos, C.M. (1992), "A simple numerical technique for turbulent flows with free surfaces." *Int. J. Numer. Meth. Fluids*, 15, 127– 146.

Lin, P.Z., and Liu, P.L.-F. (1998a), "A numerical study of breaking wave in the surf zone." *J. Fluid Mech.*, 359, 239–264.

Lin, P.Z., Liu, P.L.-F. (1998b), "Turbulence transport, vorticity dynamics, and solute mixing under plunging breaking waves in surf zone." *J. Geophys. Res.*, 103, 15677– 15694.

Liu, X.D., Osher, S. and Chan, T. (1994). "Weighted essentially non-oscillatory schemes." *J. Comput. Phys,*115, 200-212.

Miyata, H. (1986). "Finite-difference simulation of breaking waves." *J. Comput. Phys.*, 65, 179- 214.

Nichols, B.D., Hirt, C.W., and Hotchkiss, R.S. (1980). "SOLA-VOF: A solution algorithm for transient fluid flow with multiple free boundaries." *Los Alamos Scientific Laboratory*, LA-8355, UC-32 and UC-34.

Onorato, M., Osborne, A.R., and Serio, M. (2006). "Modulation instability in crossing sea states: A possible mechanism for the formation of freak waves." Phys. Rev. Lett., 96, 014503.

Osher, S., and Fedkiw R. (2003). *Level set methods and dynamic implicit surfaces*. Springer, Verlag, New York.

Osher, S., and Sethian, J.A. (1988). "Fronts propagating with curvature-dependent speed: algorithms based on Hamilton–Jacobi formulations." *J. Comput. Phys.*, 79(1), 12-49.

Peng, D., Merriman, B., Osher, S., Zhao, H.-K., and Kang, M. (1999). "A PDE-based fast local level set method." *J. Comput. Phys*., 155, 410–438.

Petit, H.A.H., van Gent, M.R.A., and van den Boscj, P. (1994). "Numerical simulation and validation of plunging breakers using a 2D Navier-Stokes model." *Proc., 24th International Conference on Coastal Eng,* ASCE, Kobe, Japan, 511 –524.

Pontaza, J.P., Chen, H.C., and Reddy, J.N. (2005). "A local analytic based discretization procedure for the numerical solution of incompressible flows." *Int. J. Numer. Meth. Fluids*, 49(6), 657-699.

Pruett, C.D., and Chang C.L. (1995). "Spatial direct numerical simulation of high-speed boundary-layer flows-part ii: Transition on a cone in Mach 8 flow." *Theor. Comput. Fluid Dyn.*, 7, 397–424.

Sethian, J A. (2001). "Evolution, implementation, and application of level set and fast marching methods for advancing fronts." *J. Comput. Phys.*, 169, 503-555.

Sussman, M., and Fatemi, E. (1999). "An efficient, interface-preserving level set redistancing algorithm and its application to interfacial incompressible fluid flow." SIAM J. Sci. Comp, 20, 1165-1191.

Sussman, M., Fatemi, E., Smereka, P., and Osher, S. (1998). “An improved level set method for imcompressible two-phase flows." *Computer & Fluids*, 27, 663-680.

Sussman, M., Smereka, P., and Osher, S.J. (1994). “A level set approach to computing solutions to incompressible two-phase flow.” *J. Comput. Phys.,* 114, 146–59.

Tome, M. F., and McKee, S. (1994). “GENSMAC: A computational marker and cell method for free-surface flows in general domains.” *J. Comput. Phys.*, 110(1), 171–186.

Unverdi, S.O., and Tryggvason G. (1992). “A front-tracking method for viscous, incompressible, multi-fluid flows.” *J. Comput. Phys.*, 100(1), 25-37.

Yu, K., Chen, H.C., Kim, J.W., and Lee, Y.B. (2007). “Numerical simulation of two-phase sloshing flow in LNG tank using finite-analytic level-set method.” *26th International Conference on Offshore Mech. and Arctic Eng.*, San Diego, CA, paper 2007-29745.

Yue, W.S., Lin C.L., and Patel V.C. (2003). “Numerical simulation of unsteady multidimensional free surface motions by level-set method.” *Int. J. Numer. Meth. Fluids*, 42, 853–884.

Wasistho, B., Geurts, B.J., and Kuerten, J.G.M. (1997). “Simulation techniques for spatially evolving instabilities in compressible flow over a flat plate.” *Computers and Fluids*, 26(7), 713-739.

Wijayaratna, N., and Okayasu, A. (2000). “DNS of wave transformation, breaking and run-up on sloping beds.” *Proc., 4th Int. Conf. on Hydrodynamics*, vol. 2. IAHR, Yokohama, Japan, 527– 532.

Zalesak, S.T. (1979). “Fully multidimensional flux-corrected transport algorithms for fluids." *J. Comput. Phys.*, 31, 335-362.

Zhao, Q., and Tanimoto, K. (1998). "Numerical simulation of breaking waves by large eddy simulation and VOF method." *Proc., 26th International Conference on Coastal Eng.*, ASCE, Copenhagen, Denmark, 892– 905.

VITA

Qian Dong received her Bachelor of Science degree in Water Resource and Ocean Engineering from Zhejiang University in 2007. She entered her Masters program in Civil Engineering at Texas A&M University in September 2008, and started her internship at ABS in the Research & Product Development department from December 2009 to May 2010. She graduated from TAMU with her M.S. in May 2010. Her research interests include numerical simulation of flow/structure interaction.

Ms. Dong may be reached at Department of Civil Engineering, Texas A&M University, 3136 TAMU, College Station, TX 77843-3136, USA. Her email is dongqian2008@neo.tamu.edu.